Acceleration of tropical cyclone development by cloud-radiative feedbacks

Allison A. Wing*

Department of Earth, Ocean and Atmospheric Science, Florida State University, Tallahassee, Florida

**Corresponding author*: Allison A. Wing, awing@fsu.edu

Early Online Release: This preliminary version has been accepted for publication in *Journal of the Atmospheric Sciences* cited, and has been assigned DOI 10.1175/JAS-D-21-0227.1. The final typeset copyedited article will replace the EOR at the above DOI when it is published.

ABSTRACT

A complete understanding of the development of tropical cyclones (TC) remains elusive and forecasting TC intensification remains challenging. This motivates further research into the physical processes that govern TC development. One process that has, until recently, been under-investigated is the role of radiation. Here, the importance of radiative feedbacks in TC development and the mechanisms underlying their influence is investigated in a set of idealized convection-permitting simulations. A TC is allowed to form after initialization from a mesoscale warm, saturated bubble on an f-plane, in an otherwise quiescent and moist neutral environment. Tropical storm formation is delayed by a factor of two or three when radiative feedbacks are removed by prescribing a fixed cooling profile or spatially homogenizing the model-calculated cooling profiles. The TC's intensification rate is also greater when longwave radiative feedbacks are stronger. Radiative feedbacks in the context of a TC arise from interactions between spatially and temporally varying radiative heating and cooling (driven by the dependence of radiative heating and cooling rate on clouds and water vapor) and the developing TC (the circulation of which shapes the structure of clouds and water vapor). Further analysis and additional mechanism denial experiments pinpoint the longwave radiative feedback contributed by ice clouds as the strongest influence. Improving the representation of cloud-radiative feedbacks in forecast models therefore has the potential to yield critical advancements in TC prediction.

Accepted for publication in *Journal of the Atmospheric Sciences.* DOI 10.1175/JAS-D-21-0227.1.

Significance statement. Our understanding of the development of tropical cyclones, hurricanes, and typhoons is incomplete, and forecasting tropical cyclone formation and intensification remains challenging. This study investigates the importance of interactions between clouds and solar and infrared radiation for tropical cyclone development. I find that in idealized convection-permitting simulations, tropical cyclone development is accelerated by a factor of two or more with the inclusion of these cloud-radiation feedbacks. The interaction of ice clouds associated with strong thunderstorms with infrared radiation has the biggest effect. These results indicate that improving the representation of ice clouds and their radiative feedbacks in forecast models has the potential to yield critical advancements in tropical cyclone prediction.

1. Introduction

A complete understanding of the process of tropical cyclone (TC) development remains elusive. As one of the largest gaps in our knowledge of tropical meteorology, the lack of a fundamental theory for TC genesis impedes progress in improving forecast models and contributes to low confidence in future projections of TC activity (Knutson et al. (2020), and references therein). Further, while there has been progress in the prediction of TC intensity, challenges, especially regarding forecasting rapid intensification, still remain (e.g., DeMaria et al. 2014; Cangialosi et al. 2020; Trabing and Bell 2020; DeMaria et al. 2021). Consequently, there is strong motivation for further research into the physical processes that govern TC development.

Much of the recent interest in the impact of radiation on TCs was spurred by the discovery of a pronounced diurnal variation in TC structure, first observed as outward propagating pulses in the infrared cloud-top brightness temperature field tied to the "diurnal clock" (e.g., Kossin 2002; Dunion et al. 2014; Wu and Ruan 2016; Knaff et al. 2019; Ditchek et al. 2019a,b, 2020), and subsequently also identified in low-level inflow (Zhang et al. 2020). Numerical simulations

Accepted for publication in *Journal of the Atmospheric Sciences*. DOI 10.1175/JAS-D-21-0227.1.

indicate that these oscillations may be a result of diurnal fluctuations of radiative heating in the TC outflow layer that drive radially propagating wave signals through a deep layer of the troposphere (Navarro and Hakim 2016; Zhou et al. 2016; O'Neill et al. 2017; Navarro et al. 2017; Ruppert and O'Neill 2019; Evans and Nolan 2019; Dunion et al. 2019). In particular, the diurnal cycle has been suggested to accelerate TC genesis and intensification in numerical simulations (Hobgood 1986; Craig 1996; Ge et al. 2014), in which strong nighttime longwave cooling is thought to destabilize the local and large-scale environment, promoting deep convection and TC development. Indeed, when nighttime cooling is absent, genesis of Hurricane Karl (2010) and Hurricane Edouard (2014) in case study simulations was suppressed (Melhauser and Zhang 2014; Tang and Zhang 2016). The formation of secondary eyewalls and the contraction of the radius of maximum wind during the intensification of Hurricane Edouard (2014) were also shown to be sensitive to the diurnal radiation contrast (Tang et al. 2017, 2019; Trabing and Bell 2021). Idealized modeling studies provide additional evidence that cloud-radiation interactions modulate TC structure, motion, and intensity (Fovell et al. 2010, 2016; Bu et al. 2014; Trabing et al. 2019; Rios-Berrios 2020).

While these previous studies provide ample evidence that radiation influences TCs, I focus on the impact of radiative *feedbacks* on TC genesis and intensification, rather than the mere existence of radiative processes. TC radiative feedbacks result from interactions between spatially and temporally varying radiative heating and cooling and the developing tropical cyclone, driven by the dependence of the radiative heating rate on clouds and water vapor. Radiation affects tropical cyclones, and more generally, deep moist convection, in multiple ways. Vertical gradients in radiative cooling between cloud top and cloud base locally influence atmospheric stability (Hobgood 1986) and horizontal gradients of radiative cooling between areas of deep convection and surrounding cloud-free regions increase clustering of convection and column moist static energy (MSE) within the incipient storm (Wing et al. 2016). These spatial differences in heating also generate a circu-

Accepted for publication in *Journal of the Atmospheric Sciences*. DOI 10.1175/JAS-D-21-0227.1.

lation response (Gray and Jacobson 1977) that favors TC development (Nicholls 2015; Muller and Romps 2018) by enhancing the convergence of angular momentum and promoting saturation of the storm core, thus shortening the gestation period before genesis and rapid intensification (Ruppert et al. 2020).

Feedbacks resulting from anomalous radiative heating in areas of deep convection relative to the TC's surroundings have a substantial impact on TC development in idealized simulations. These results follow from the discovery of self-aggregation of convection in simulations of radiative-convective equilibrium (RCE), an idealization of the tropical atmosphere in which there is a statistical balance between radiative cooling and convective heating (Held et al. 1993). Self-aggregation of convection, in which convection spontaneously organizes into coherent clusters despite homogeneous boundary conditions and forcing (see Wing et al. (2017) for a review), results from an instability driven primarily by cloud-radiative feedbacks (e.g., Bretherton et al. 2005; Muller and Held 2012; Wing and Emanuel 2014). These same cloud-radiative feedbacks accelerate spontaneous TC genesis in RCE simulations in a rotating environment (Davis 2015; Wing et al. 2016; Muller and Romps 2018; Carstens and Wing 2020; Yang and Tan 2020).

Building on studies of self-aggregation, radiative feedbacks were also found to accelerate TC development from an idealized initial disturbance (Smith et al. 2020; Wu et al. 2021) and in case study simulations of observed, archetypal TCs (Ruppert et al. 2020; Yang et al. 2021). They also contribute to TC development in global climate models, particularly in early stages of development and in weaker storms (Wing et al. 2019), where suppressing radiative interactions significantly reduces global TC frequency (Zhang et al. 2021). In realistic case study simulations of Hurricane Maria (2017) and Typhoon Haiyan (2015), Ruppert et al. (2020) found that removing the cloud-radiative feedback by making clouds transparent to radiation prevents or delays TC genesis and intensification. Even when the feedback is removed after the TC has already formed and rapid

Accepted for publication in *Journal of the Atmospheric Sciences*. DOI 10.1175/JAS-D-21-0227.1.

intensification is underway, the duration of intensification is limited, indicating the important role played by the cloud-radiative feedback.

While the results of Ruppert et al. (2020) provide strong evidence for the importance of cloud-radiative feedbacks in TC development, and the common development pathway followed by Maria and Haiyan suggests the results should generalize to other storms that follow similar pathways, it is important to determine the robustness of their result beyond a few case studies. Rotating RCE simulations suggest that the importance of radiative feedbacks in TC genesis is very fundamental, since they are found to accelerate genesis when a TC is allowed to form on its own without any impositions or external influences (Wing et al. 2016; Muller and Romps 2018). However, the applicability of such extremely idealized simulations to real world TCs, which form on faster time scales from pre-existing disturbances, is unsettled. Therefore, the objective of this study is to investigate the role of radiative feedbacks in TC genesis and intensification in the middle ground between spontaneous TC genesis in rotating RCE and realistic case study simulations, This type of approach has also been taken by a few prior studies who employed an idealized initial vortex (e.g., Nicholls 2015; Smith et al. 2020; Wu et al. 2021), but here, I consider convection-permitting simulations initialized from a warm, moist bubble, which rapidly form a TC within a few days in the control simulation (Section 2). I investigate in detail the contributions of different aspects of the radiative feedback, considering the role of both longwave and shortwave radiation and the radiative effects of spatially varying water vapor, ice clouds, and liquid water clouds (Section 3). I also employ a budget for the spatial variance of column-integrated frozen moist static energy to quantify the radiative feedback (Section 4). I discuss conclusions from the study in Section 5.

Accepted for publication in *Journal of the Atmospheric Sciences*. DOI 10.1175/JAS-D-21-0227.1.

2. Model Simulations

I perform a set of simulations using the System for Atmospheric Modeling (SAM) version 6.11.2 (Khairoutdinov and Randall 2003). The original SAM one-moment microphysics scheme, a Smagorinksy sub-grid scale turbulence scheme, the original SAM advection scheme based on Smolarkiewicz' MPDATA scheme with a monotonic corrector, and the RRTMG scheme for both longwave and shortwave radiation (Mlawer et al. 1997; Clough et al. 2005; Iacono et al. 2008) are used. In the one-moment microphysics scheme, there are two prognostic water variables: total non-precipitating water (water vapor, cloud liquid water, and cloud ice) and total precipitating water (rain, snow, graupel). The cloud condensate (cloud liquid water and cloud ice) is diagnosed such that there is no supersaturation of water vapor. A temperature-based partitioning is then used to diagnose the individual hydrometeor mixing ratios from cloud condensate and total precipitating water. Note that SAM's implementation of RRTMG when used with the one-moment microphysics scheme *does not* consider the effect of precipitating hydrometeors (rain, snow, graupel) on cloud radiative and optical properties. Only non-precipitating hydrometeors (cloud liquid water and cloud ice) are radiatively active. This distinction between non-precipitating and precipitating ice is not necessarily consistent with observational retrievals nor is it consistent across other model implementations (e.g., Waliser et al. 2009). Indeed, SAM has the option to use other, more advanced, microphysics schemes (e.g., Morrison et al. 2005; Thompson et al. 2008), in which snow is radiatively active in RRTMG, but this is not explored here. While this choice may impact the results (e.g., Brown et al. 2016), using the one-moment microphysics scheme is consistent with previous studies of self-aggregation and TC formation with SAM (e.g., Bretherton et al. 2005; Muller and Held 2012; Wing and Emanuel 2014; Wing et al. 2016; Muller and Romps 2018; Carstens and Wing 2020).

Accepted for publication in *Journal of the Atmospheric Sciences.* DOI 10.1175/JAS-D-21-0227.1.

Each simulation is on a 2048 km x 2048 km domain with doubly periodic boundary conditions and horizontal grid spacing of 2 km. There are 74 vertical levels with a rigid lid at 35 km, using the grid specified by the Radiative-Convective Equilibrium Model Intercomparison Project (RCEMIP) protocol (Wing et al. 2018), and with a sponge layer in the upper third of the model domain. The time step has a maximum value of 10 s, but can vary in order to satisfy the CFL condition. The lower boundary condition is a fixed sea surface temperature of 300 K. In all but one set of simulations (discussed below) solar forcing is specified as an equinoctial (Julian Day 80.5) diurnal cycle of insolation at 20.95°N latitude, with a time-mean insolation of 409.6 W m^{-2}. This representative diurnal cycle matches the tropical (0-20°) annual mean insolation. The simulations are performed on a f-plane with the Coriolis parameter $f = 5x10^{-5}$ s^{-1}, corresponding to the value at 20°N. Surface fluxes are computed interactively from the resolved near-surface wind and thermodynamic variables, using a minimum wind speed of 1 m s^{-1} (following Wing et al. 2018) and an iterative process to compute the exchange coefficients. The inclusion of a minimum wind speed may artificially increase the surface fluxes in regions of very weak winds, thus limiting wind-driven spatial variability of surface fluxes and damping the surface flux feedback, but this is more of an issue when smaller grid spacing or larger minimum wind speeds are used (Mol et al. 2019).

The simulations are run for 10 days following initialization from a warm, moist bubble inserted into an initially calm, homogenous environment, where the environmental sounding is an average profile from a small (96 km x 96 km) domain radiative-convective equilibrium simulation, performed as part of RCEMIP (Wing et al. 2020). While the RCEMIP simulation does not have a diurnal cycle, its solar constant and zenith angle are fixed such that the insolation is 409.6 W m^{-2}, matching the time-mean insolation of the bubble simulation with diurnal cycle. The other parameters, such as the sea surface temperature and trace gas profiles, are identical in the bubble

Accepted for publication in *Journal of the Atmospheric Sciences*. DOI 10.1175/JAS-D-21-0227.1.

simulation and the RCEMIP simulation from which it is initialized. The structure of the bubble is shown in Figure 1. The center of the bubble is in the middle of the domain at a height of 4 km, has a temperature anomaly at the center of 10 K and a humidity anomaly at the center of 6.9360 g kg^{-1}; this makes the air at the center of the bubble saturated. The radius of the bubble is 2 km in the vertical and 250 km in the horizontal. These settings are similar to those used in prior studies (O'Neill et al. 2017; Fovell et al. 2010, 2016; Bu et al. 2014; Hill and Lackmann 2009a,b). Initialization from a mesoscale warm and moist bubble allows a circulation to rapidly spin-up to create a balanced circulation. In addition, since the TC genesis process is stochastic (Zhang and Sippel 2009), random white noise perturbations are added to the initial boundary layer temperature field on top of the bubble perturbation (an amplitude of 0.1 K in the lowest layer, decreasing linearly to 0.02 K in the fifth layer). This initial white noise is varied (but statistically identical) to form a 5-member ensemble for each set of simulations.

A series of mechanism-denial experiments are performed which progressively test the impact of different aspects of the radiative feedback, as summarized in Table 1. The control simulation (`CTRL`) has fully interactive radiation, in which the radiative transfer is performed using the model-computed temperature, water vapor, and cloud fields. RRTMG is called every 30 timesteps (~5 minutes). In one set of sensitivity experiments, `No-Diurnal`, the diurnal cycle is removed by specifying a reduced solar constant of 551.58 W m^{-2} and a fixed zenith angle of 42.05°, equal to the average insolation-weighted zenith angle between the Equator and 20° (Wing et al. 2018). This experiment tests the role of diurnally varying insolation, while keeping the time-mean insolation fixed. In all other simulations, the diurnal cycle is included. I employ two different methods of removing feedbacks that result from spatial variations of radiative heating rates: `Homog-Rad` and `Fix-Rad`. In `Homog-Rad`, the radiative heating rates are spatially homogenized at each level before being applied as a tendency at each radiation time step. In this way, the domain average radiative

Accepted for publication in *Journal of the Atmospheric Sciences*. DOI 10.1175/JAS-D-21-0227.1.

heating is the same as in `CTRL`, but each grid point receives identical radiative heating tendencies. This is different from previous approaches, which have often assessed the role of radiation in TC development by performing simulations with radiation turned on and turned off (e.g., Smith et al. 2020). Turning off radiation introduces a mean state difference, whereas `Homog-Rad` has the advantage of isolating the role of radiative feedbacks, specifically, rather than just the existence of radiative fluxes themselves. `Fix-Rad` removes radiative feedbacks by prescribing a specified radiative heating rate profile at all grid points and all times; this is subtly different than `Homog-Rad`, in which the mean radiative heating rate profile is allowed to evolve in time. The specified profile that is prescribed in `Fix-Rad` is drawn from the horizontal- and time-mean (over the last 20 days) of the small domain RCEMIP simulation from which the bubble simulations are initialized (Figure 2a).

The remaining sets of simulations are designed to isolate how different aspects of the radiative feedback contribute to TC development, including contributions from longwave radiation, shortwave radiation, water vapor variability, ice clouds, and liquid water clouds. In `Fix-LW`, a fixed longwave radiative heating rate profile (drawn from the small domain RCEMIP simulation; Figure 2a) is prescribed, while shortwave radiation is calculated interactively. Thus, in `Fix-LW`, only shortwave radiative feedbacks are present. Likewise, only longwave radiative feedbacks are present in `Fix-SW`, in which a fixed shortwave radiative heating rate profile (Figure 2a) is prescribed and longwave radiation is calculated interactively.

Water vapor radiative feedbacks are removed in `Fix-`q_v, `Fix-LW-`q_v, and `Fix-SW-`q_v by using a fixed, specified water vapor profile in the radiative transfer calculation of both longwave and shortwave, longwave only, and shortwave only, respectively. In `Fix-LW-`q_v, the specified water vapor profile is used in the longwave radiative transfer calculation while the simulated water vapor profile is used in the shortwave calculation. Likewise, in `Fix-SW-`q_v the specified water vapor

Accepted for publication in *Journal of the Atmospheric Sciences*. DOI 10.1175/JAS-D-21-0227.1.

profile is used in the shortwave calculation while the simulated water vapor profile is used in the longwave calculation. The specified water vapor profile is the same as that of the initial sounding (Figure 2b). Cloud-radiative feedbacks are still present in the `Fix-`q_v, `Fix-LW-`q_v, and `Fix-SW-`q_v simulations.

The final set of simulations removes cloud-radiative feedbacks by zeroing the cloud condensate inputs to the radiative transfer calculation; this is equivalent to making the simulated clouds transparent to radiation. `Zero-`q_{cl}, q_{ci} zeros both liquid and ice clouds, `Zero-`q_{cl} zeros liquid clouds only (retaining the radiative influence of ice clouds), and `Zero-`q_{ci} zeros ice clouds only (retaining the radiative influence of liquid clouds). Precipitating ice (snow and graupel) are *not* radiatively active in this configuration of SAM, and thus `Zero-`q_{cl}, q_{ci} and `Zero-`q_{ci} only zero non-precipitating cloud ice. The water vapor radiative feedback is still present in all the zeroed-cloud simulations.

3. Results

a. Role of Radiative Feedbacks

After initialization, the model rapidly adjusts to the bubble perturbation to create a weak vortex. In the set of `CTRL` simulations, a tropical cyclone quickly forms and rapidly intensifies within the first few days of the simulation, showing the effectiveness of the bubble initialization in quickly generating a TC. The intensity V_{max} is assessed based on the maximum azimuthal mean tangential wind at the lowest model level (37 m). The cyclone center is tracked according to the location of minimum pressure at the lowest model level and hourly instantaneous snapshots of the horizontal wind are interpolated to radial coordinates based on this center, following the approach of Wing et al. (2016). After the first day, the tracked center stays close to the center of the domain (where the

Accepted for publication in *Journal of the Atmospheric Sciences*. DOI 10.1175/JAS-D-21-0227.1.

initial bubble perturbation was centered) in all simulations. On average across the CTRL ensemble, V_{max} reaches tropical storm strength (18 m s^{-1}) at day 3.23, hurricane strength (33 m s^{-1}) at day 3.72, and its lifetime maximum intensity (LMI) at day 5.02 (Table 2, Figure 3). There is then a gradual decline in V_{max} in the remaining 5 days of the simulation, though the storm remains a strong hurricane. This is not surprising because it is common in numerical simulations for TCs to "overshoot" their steady state intensity, and I do not expect that the simulated TCs have reached steady state, given the short duration of the simulation (Hakim 2011). However, since my objective is to examine the formation and intensification of the TC, the 10-day simulation is suitable for the purposes of this study. All CTRL ensemble members behave similarly, with a range of time to tropical storm and hurricane strength of ~8 hours and range of time to the LMI of ~16 hours across the ensemble (Table 2).

Removing the diurnal cycle has little effect on TC development in these simulations. The average times to tropical storm strength, hurricane strength, and LMI are slightly shorter in No-Diurnal compared to CTRL (Table 2), but this is not significant relative to the ensemble spread (Figure 3a). This result is in agreement with some prior work (Ruppert and O'Neill 2019; Trabing and Bell 2021), but is in opposition to other work that, while not necessarily framed in terms of radiative feedbacks, has suggested that the diurnal cycle accelerates TC development (Melhauser and Zhang 2014; Tang and Zhang 2016). The diverging results in the literature could be due to the unique case studies considered, but they are more likely due to the method of removing the diurnal cycle. Here, as in Ruppert and O'Neill (2019), the diurnal cycle was removed by keeping the sun "on" all the time, but at a reduced insolation such that the time-mean insolation was unchanged compared to CTRL. Melhauser and Zhang (2014) and Tang and Zhang (2016) instead found suppressed TC formation under conditions of perpetual local noon, which would introduce a substantial difference in the mean state. This emphasizes the importance of the methodology by which possible radiative

Accepted for publication in *Journal of the Atmospheric Sciences*. DOI 10.1175/JAS-D-21-0227.1.

feedbacks are removed. My results indicate that the presence of diurnally varying insolation does not, on its own, accelerate TC genesis or intensification. It remains possible that the diurnal cycle could influence other aspects of TC structure or evolution, such as favoring intensification during a particular time of day (Wu et al. 2020), but I do not investigate the `No-Diurnal` simulations further here.

Removing radiative feedbacks via `Homog-Rad` and `Fix-Rad` substantially delays TC formation and slows TC intensification (Figure 3). While the ensemble spread in the evolution of V_{max} is somewhat larger in `Homog-Rad` and `Fix-Rad` than in `CTRL`, it is clear that the simulations without radiative feedbacks are outside the range of possible outcomes with radiative feedbacks. The average time to hurricane strength is more than twice as long in both `Homog-Rad` and `Fix-Rad` than it is in `CTRL` (Table 2). If the TC intensity is instead defined based on the maximum lowest model level wind speed found anywhere in the domain, the wind speed values are higher and the `CTRL`, `Homog-Rad` and `Fix-Rad` curves diverge a bit later (around day 2) than in Figure 3 but the conclusion about the impact of radiative feedbacks on TC development is unchanged (see Figures S1-S2 in the supplementary material). Removing radiative feedbacks via `Fix-Rad` is slightly more effective at delaying TC development than `Homog-Rad`, but overall the two approaches yield similar results. One of the `Homog-Rad` ensemble members reaches its LMI right at the end of the simulation, indicating that the actual time to LMI is likely a bit longer than 10 days.

Figure 4 shows the evolution of convection and moisture in the first five days for the simulations with and without radiative feedbacks (`CTRL` and `Homog-Rad`). Here I examine outgoing longwave radiation (OLR) as an indicator of cold cloud tops, which may result from deep convection, but remind the reader that the thermodynamic equation in `Homog-Rad` is not aware of this variability in radiative fluxes, as it is the horizontal-mean radiative heating tendencies that are applied. The evolution in `Fix-Rad` is not shown, since the radiative heating tendencies are prescribed and OLR

Accepted for publication in *Journal of the Atmospheric Sciences*. DOI 10.1175/JAS-D-21-0227.1.

is not computed, but the precipitable water field is similar to that in `Homog-Rad`. By day 2 in `CTRL`, convection and moisture have aggregated at the center of the domain and a circulation is apparent. Over the next several days as deep convection associated with the developing TC becomes deeper (lower OLR associated with taller, colder cloud tops) and more organized, the precipitable water increases within the TC and decreases in the environment surrounding the TC. Without radiative feedbacks, the amplification of moisture anomalies is stunted (Figure 4p-t). Slightly higher values of precipitable water are apparent at the center of the domain at day 3 in `Homog-Rad`, but they exhibit only a slight increase over the next few days, in contrast to the rapid growth of moisture anomalies in `CTRL`. Associated with this, the convection in `Homog-Rad` takes longer to organize and remains shallow through day 5. The appearance of the OLR and precipitable water fields in `Homog-Rad` at day 5 are qualitatively similar to that in `CTRL` at day 2 of the simulation, emphasizing that without radiative feedbacks, TC development is delayed by a factor of two or more.

b. Decomposition of Radiative Feedbacks

Section 3a showed that the presence of radiative feedbacks accelerates TC development, compared to an ensemble of simulations in which those feedbacks were removed. These radiative feedbacks result from spatiotemporal variability in radiative heating rates, which in turn result from spatiotemporal variability in water vapor and cloud content and affect both shortwave and longwave radiation. Figure 5a decomposes the total radiative feedback into contributions from shortwave and longwave radiation, by comparing `CTRL` and `Fix-Rad` to `Fix-LW` and `Fix-SW`. The ensemble of `Fix-SW` simulations, in which shortwave feedbacks are removed but longwave feedbacks are still present, is close to that of `CTRL`, but shifted slightly earlier (see also Table 2). The ensemble of `Fix-LW` simulations, in which longwave feedbacks are removed but shortwave feedbacks are still present, overlaps with the `Fix-Rad` ensemble and results in TC development

Accepted for publication in *Journal of the Atmospheric Sciences*. DOI 10.1175/JAS-D-21-0227.1.

that is delayed compared to CTRL. These results combined indicate that it is *longwave* radiative feedbacks that are responsible for acceleration of TC development. While there is overlap between the Fix-LW and Fix-Rad ensembles, the Fix-LW ensemble mean indicates slightly slower TC development than Fix-Rad. This could indicate that the shortwave feedback on its own (as the only radiative feedback present in Fix-LW) is detrimental to TC development. A possible explanation for this is that deep convective clouds in the incipient storm reflect shortwave radiation before it can enter the atmosphere and be absorbed by water vapor. This effect can be seen in Figure 6a, in which the clear-sky column shortwave heating (black dash-dot line) is larger near the TC center but the all-sky column shortwave heating (solid black line) is smaller near the TC center. The reduction in column shortwave heating in the moist convecting areas near the TC relative to the non-convecting areas acts as a negative feedback on moist static energy variance, disfavoring convective aggregation and TC development. Quantification of the shortwave feedback in Section 4 indicates that it is indeed slightly negative just after tropical storm formation due to the effects of clouds (not shown), but it is orders of magnitude smaller than any other feedbacks so it is unlikely to provide a meaningful contribution. Therefore, the slightly slower TC development in Fix-LW compared to Fix-Rad, and the slightly quicker TC development in Fix-SW compared to CTRL, could instead be due to differing evolution of other factors (such as the moisture distribution) or simply random variability.

Since radiative feedbacks depend on the spatiotemporal distribution of both water vapor and clouds, Figures 5b-c separately remove water vapor feedbacks and cloud feedbacks to determine which contributes more to the acceleration of TC development. When radiative heating rates are calculated based on a prescribed profile of water vapor, rather than the spatiotemporally varying water vapor calculated by the model integration, the TC development is similar to that in CTRL (Figure 5b). This is true regardless of whether prescribed water vapor profile is used

Accepted for publication in *Journal of the Atmospheric Sciences*. DOI 10.1175/JAS-D-21-0227.1.

for the calculation of shortwave radiation, longwave radiation, or both. Note that in Fix-q_v, Fix-LW-q_v, and Fix-SW-q_v water vapor is only fixed in the radiative transfer calculation, it is still a prognostic variable in the model. Therefore, these experiments isolate the effect of the water vapor - radiation feedback and should not be interpreted as an indication of the role of moisture in TC development overall. When cloud-radiative feedbacks are removed in Zero-q_{cl},q_{ci} by making all clouds transparent to radiation, TC development is delayed compared to CTRL, and it is delayed nearly as much as when all radiative feedbacks are removed (Homog-Rad or Fix-Rad; Table 2). When liquid and ice clouds are zeroed in the radiative transfer calculation separately, neither on its own has as large an effect on TC development as zeroing both at the same time (Figure 5c; also discussed further below and in Figure 9). Zero-q_{ci} exhibits greater ensemble spread and a slower TC intensification rate than Zero-q_{cl} or CTRL (7.25 m $s^{-1}d^{-1}$ compared to 21.82 m $s^{-1}d^{-1}$ and 24.42 m $s^{-1}d^{-1}$, respectively). This suggests that ice clouds contribute more to the TC cloud-radiative feedback than liquid clouds do, even though Zero-q_{ci} only has a slight, though statistically significant, delay in TC formation compared to CTRL. This is discussed further below, in Figures 6-8, and in Sections 4-5.

The relative impacts of water vapor and ice and liquid clouds can be further understood by examining the spatial variability in radiative heating. Figure 6 considers the azimuthal mean column shortwave (N_S) and longwave (N_L) flux convergences averaged over days 3-4, which is a time period in which the TC is rapidly intensifying in some simulations and just beginning to develop in others. N_S and N_L represent how much the atmospheric column is heating or cooling via shortwave and longwave radiation, respectively, and enter into the calculation of the radiative feedbacks in Section 4. Since I showed above that the total radiative feedback is dominated by longwave effects and the radial variability of N_S is much smaller than N_L (compare y-axis scale in panel (a) vs. panel (b) in Figure 6), I focus on the longwave variability. However, I briefly note

Accepted for publication in *Journal of the Atmospheric Sciences*. DOI 10.1175/JAS-D-21-0227.1.

that the radial gradient of N_S in $\texttt{Zero-q}_{\text{ci}}$, which has transparent ice clouds, is opposite that in the simulations that have radiatively active ice clouds (that is, N_S increases towards the TC center rather than decreases; compare cyan line to black, green, and gray dashed lines in Figure 6a). This enhancement of the column shortwave heating due to moist air and liquid clouds near the TC center when there is no reflection or absorption of shortwave radiation by ice clouds may contribute to the faster TC development in $\texttt{Zero-q}_{\text{ci}}$ compared to $\texttt{Zero-q}_{\text{cl}},\text{q}_{\text{ci}}$ that I noted above. In CTRL, there is a large radial gradient in N_L (varying by nearly 100 Wm^{-2} over 500 km), with less cooling near the TC center. This is due almost entirely to cloud radiative effects; the equivalent N_L computed with clear-sky fluxes (black dash-dot line in Figure 6b) has only a small radial gradient (remaining near -200 Wm^{-2} across all radii). Consistent with this, in $\texttt{Fix-q}_v$ the spatial variability in N_L is very similar to that in CTRL, whereas in $\texttt{Zero-q}_{\text{cl}},\text{q}_{\text{ci}}$, N_L is similar to the clear-sky N_L in CTRL and has a weak radial gradient. The radial gradient in N_L is weak in $\texttt{Zero-q}_{\text{ci}}$ (comparable to $\texttt{Zero-q}_{\text{cl}},\text{q}_{\text{ci}}$) and strong in $\texttt{Zero-q}_{\text{cl}}$ (comparable to CTRL, though with slightly less cooling on average). The comparison of N_L across the different simulations indicates that ice clouds dominate the spatial variability in column longwave cooling.

The anomaly of the azimuthal mean longwave radiative heating rate from its radius-weighted mean across all radii, as a daily average over each of the first five days of simulation, provides information on the temporal evolution of both the vertical and radial structure of the radiative impacts of ice and liquid clouds (Figure 7). An equivalent figure for shortwave radiative heating rate can be found in the supplementary material (Figure S3), as can a version that shows an instantaneous snapshot of the longwave heating rate anomalies (Figure S4). The latter indicates similar, but noisier, patterns as in Figure 7. In CTRL substantial radial anomalies are evident by day 2, with anomalous longwave cooling at the top of the deep convective clouds near the TC center and anomalous longwave warming below throughout most of the depth of the troposphere

Accepted for publication in *Journal of the Atmospheric Sciences*. DOI 10.1175/JAS-D-21-0227.1.

and the boundary layer. This pattern amplifies as the TC becomes better organized and intensifies through days 3-5. Overall, there is anomalous warming between the surface and ~10-14 km within ~200-400 km of the TC center, compared to anomalous cooling above ~10-14 km and outwards of ~200-400 km. In contrast, there are negligible radial anomalies in the longwave heating rate in Zero-q_{cl},q_{ci}, emphasizing the importance of clouds in driving the spatial variability in radiative heating. Consistent with Figure 6, ice clouds contribute the most to the structure of the longwave anomalies in Figure 7; much of the spatial variability in longwave heating rates in CTRL (Figure 7a-e) is recovered by Zero-q_{cl}, in which *only* ice clouds are radiatively active (Figure 7p-t). This is consistent with the slower TC intensification rate in Zero-q_{ci} compared to Zero-q_{cl}. Ice clouds drive both local and remote radiative effects, the latter demonstrated by anomalous warming in the lower and mid-troposphere (~0-5 km) far below altitudes at which ice clouds are present (~5-16 km). In Zero-q_{ci}, in which ice clouds are transparent and only liquid clouds are radiatively active, the radiative heating anomalies are weaker and less widespread. The anomalies are confined to altitudes at and below where liquid clouds are present (0-7 km), and a narrower range of radii (~0-100 km) experiences anomalous lower-tropospheric warming compared to Zero-q_{cl}. This is important because Ruppert et al. (2020) showed that it was the local warming of the lower-mid troposphere relative to the TC's surroundings that strengthened the overturning circulation of the developing storm and promoted saturation and ascent within its core. My results indicate that in these idealized simulations, a large fraction of that lower-mid tropospheric warming comes from the radiative effects of ice clouds. Consistent with this, simulations with ice cloud-radiative feedbacks removed take longer to approach saturation throughout the column and develop low-level inflow (Figure 8). Across simulations, sustained low-level inflow develops at about the same time that the troposphere is nearly saturated (i.e., ~ day 3 for CTRL). The low-level inflow is also weaker at any given time in simulations without ice cloud-radiative feedbacks. In addition to taking longer

Accepted for publication in *Journal of the Atmospheric Sciences*. DOI 10.1175/JAS-D-21-0227.1.

to saturate the inner core, simulations without ice cloud-radiative feedbacks take longer to dry out in the outer TC environment (see Figure S5 in the supplemental material). My results are thus consistent with Ruppert et al. (2020)'s argument that cloud-radiative feedbacks (here shown to be driven primarily by ice) help to strengthen the TC's overturning circulation (see also Figure S6 in the supplemental material).

While Figures 6b and 7 make clear that most of the spatial variability in longwave radiative heating rates can be attributed to the effect of ice clouds, the fact that zeroing ice and liquid clouds separately has a smaller effect on TC development than zeroing both at the same time (Figure 5c) indicates that a non-linear interaction between the radiative effects of ice and liquid clouds may also play a role. I use the factor separation method of Stein and Alpert (1993) to diagnose the non-linear interaction between ice and liquid clouds, considering them as a two independent factors. Given simulations that include both factors (CTRL), exclude both factors ($\texttt{Zero-}q_{cl}, q_{ci}$), and exclude each factor individiually ($\texttt{Zero-}q_{cl}$ and $\texttt{Zero-}q_{ci}$) the non-linear interaction is given by

$$\text{Non Linear} = \texttt{CTRL} - (\texttt{Zero-}q_{cl} + \texttt{Zero-}q_{ci}) + \texttt{Zero-}q_{cl}, q_{ci} \tag{1}$$

and the linear sum of the two factors is given by

$$\text{Linear Sum} = \texttt{Zero-}q_{cl} + \texttt{Zero-}q_{ci} - \texttt{Zero-}q_{cl}, q_{ci}. \tag{2}$$

Equivalently, the non-linear interaction is given by the difference between CTRL and the linear sum. Figure 9 compares the radial longwave heating anomalies in CTRL, the linear sum of ice and liquid clouds (Equation 2), and the non-linear interaction between ice and liquid clouds (Equation 1). The longwave heating anomalies in CTRL are well captured by the linear sum, while the non-linear interaction term has less of a clear structure. In particular, most of the important lower-mid tropospheric warming is captured, though slightly over-estimated, by the linear sum. However, the

Accepted for publication in *Journal of the Atmospheric Sciences*. DOI 10.1175/JAS-D-21-0227.1.

non-linear interaction term is in some places similar in magnitude to the linear sum and CTRL; in particular, above the freezing level (~4.5 km) in the region of mixed-phase clouds (~5-7.5 km) and near the tops of the ice clouds (~15 km). The non-linear interaction term also reflects that cloud radiative effects depend on the background distribution of other cloud types and the water vapor distribution, which evolves differently in the different simulations. It is also worth noting that, through day 3, the largest radiative heating anomalies are confined inward of the radius of maximum winds, which would allow for the low-level inward flow response to be efficient in converging angular moment towards the storm center (Vigh and Schubert 2009; Musgrave et al. 2012). There may also be a feedback by liquid clouds on the local cloud-scale circulation that is hidden by the azimuthal averages in Figures 6 and 7. While most of the storm-scale variability in the column radiative flux convergence CTRL is driven by ice clouds and thus recovered by Zero-q_{cl}, the presence of liquid clouds in Zero-q_{ci} does contribute cloud-scale variability (see Figure S7 in the supplemental material).

Overall, these results show that it is spatial variability in longwave radiative heating rates, which clouds are unequivocally responsible for, that accelerates TC development. Ice clouds contribute most of the spatial variability in longwave radiative heating rates, though there are also some contributions from liquid clouds and from the non-linear interaction between ice and liquid clouds.

4. Feedback Analysis

In order to quantify the strength of the longwave radiative feedback, I compute a budget for the spatial variance of column-integrated frozen moist static energy (FMSE). First introduced by Wing and Emanuel (2014) to quantify the physical mechanisms leading to convective self-aggregation, this budget has also been used in idealized (Wing et al. 2016; Muller and Romps 2018) and realistic (Ruppert et al. 2020; Wu et al. 2021) convection-permitting and global climate model (Wing et al.

Accepted for publication in *Journal of the Atmospheric Sciences*. DOI 10.1175/JAS-D-21-0227.1.

2019; Zhang et al. 2021) simulations of tropical cyclones. The mass-weighted column integral of FMSE, $\widehat{h}$, is given by

$$\widehat{h} = \int_0^{z_{top}} (c_p T + gz + L_v q - L_f q_{ice}) \rho dz, \tag{3}$$

where c_p is the specific heat of dry air at constant pressure, L_v is the latent heat of vaporization, q is the water vapor mixing ratio, L_f is the latent heat of fusion, and q_{ice} is the mixing ratio of all ice phase condensates (cloud ice, snow, graupel). FMSE is approximately conserved under moist adiabatic displacements, including the freezing and melting of precipitation, and its column integral is unchanged by convection. The domain-mean spatial variance of $\widehat{h}$, $\langle \widehat{h'}^2 \rangle \equiv \mathrm{var}(\widehat{h})$, which is a measure of the spread in the spatial distribution of $\widehat{h}$, increases as convection organizes and the TC develops. Var($\widehat{\mathrm{h}}$) is highly correlated with the intensity of the TC up until the time of the LMI, indicating that it is an effective measure for the local warming and moistening that characterizes TC development (Figure 10). While var($\widehat{\mathrm{h}}$) and TC intensity are correlated in all simulations, there is not a universal relationship between them. That is, there can be different values of var($\widehat{\mathrm{h}}$) for a given TC intensity across the different simulations and the slopes are different, indicating that different simulations have a different rate of var($\widehat{\mathrm{h}}$) increase associated with intensity increase. This may be because the different simulations have different physics, since various aspects of the radiative feedbacks are removed in each. However, the var($\widehat{\mathrm{h}}$)-intensity relationship is very similar between `CTRL` and `Homog-Rad` (Figure 10a), which have the same domain-mean radiative heating rates (recall that only the spatial variability is removed in `Homog-Rad`). Thus it is also possible that the variability in the var($\widehat{\mathrm{h}}$)-intensity relationship across the other simulations could be a result of a modest difference in the mean state due to the adjustments made to the radiative heating. For example, var($\widehat{\mathrm{h}}$) is expected to be lower, all else equal, in a simulation that is on average cooler, due to the Clausius-Clapeyron dependence of water vapor on temperature.

Accepted for publication in *Journal of the Atmospheric Sciences*. DOI 10.1175/JAS-D-21-0227.1.

The direct contribution of longwave and shortwave radiative feedbacks to the increase in $\mathrm{var}(\widehat{h})$, and thus TC development, can then be quantified using the budget for $\mathrm{var}(\widehat{h})$, following Wing et al. (2016), given by:

$$\frac{d\mathrm{var}(\widehat{h})}{dt} = 2\langle \widehat{h}' F_K' \rangle + 2\langle \widehat{h}' N_S' \rangle + 2\langle \widehat{h}' N_L' \rangle - 2\langle \widehat{h}' \nabla_h \cdot \widehat{\mathbf{u}h} \rangle, \tag{4}$$

where F_K is the surface enthalpy flux, N_S is the column shortwave flux convergence, N_L is the column longwave flux convergence, and $-\nabla_h \cdot \widehat{\mathbf{u}h}$ is the horizontal convergence of the density-weighted column integral of the flux of FMSE (also called the advective term). Primes indicate an anomaly from the horizontal mean, $\langle A \rangle$, where A is any quantity. Each term on the right hand side of Equation 4 represents a feedback on $\mathrm{var}(\widehat{h})$ and TC development, in which the anomalies of $\widehat{h}$ are multiplied by anomalies in a source or sink of $\widehat{h}$. Thus, if there is an anomalous source of $\widehat{h}$, such as anomalous longwave heating, in the same location as anomalously high $\widehat{h}$ (moister than average), this is a positive feedback (in this example, a positive longwave feedback) that amplifies the $\widehat{h}$ anomalies and contributes to convective organization and TC development. Note that the advective feedback is defined with the leading negative sign; thus, if $-2\langle \widehat{h}' \nabla_h \cdot \widehat{\mathbf{u}h} \rangle > 0$, there is a positive advective feedback, contributing to an increase in $\mathrm{var}(\widehat{h})$. $2\langle \widehat{h}' N_S' \rangle$ and $2\langle \widehat{h}' N_L' \rangle$, the shortwave and longwave feedbacks, only represent the *direct* contribution of radiation to the $\mathrm{var}(\widehat{h})$ tendency. Radiative heating rate anomalies also drive circulations which may in turn contribute to the $\mathrm{var}(\widehat{h})$ tendency via advective fluxes (Muller and Held 2012; Muller and Romps 2018; Naumann et al. 2019). This *indirect* effect of radiation would be embedded within the advective term (along with advection by other circulations). Here, I focus on the direct radiative feedbacks, as a measure of how strong the co-variability between $\widehat{h}$ and column radiative flux convergence is across the different simulations with various aspects of the radiative feedback removed.

Accepted for publication in *Journal of the Atmospheric Sciences*. DOI 10.1175/JAS-D-21-0227.1.

The domain-mean var($\widehat{h}$) budget in the CTRL ensemble is similar to that in spontaneous TC genesis (Wing et al. 2016; Carstens and Wing 2022), in which the longwave and surface flux feedbacks are both positive and thus both contribute to var($\widehat{h}$) growth in the early stages of TC development, then the surface flux feedback increases in magnitude as the TC intensifies (Figure 11a). The ratio of the longwave to surface flux feedback is largest in the early stages (not shown), indicating that the relative contribution of the longwave feedback is strongest then. However, the longwave feedback remains important, with a value about a third of that of the surface flux feedback as the TC reaches its LMI. The shortwave feedback is very small, and the contribution from advection is a negative feedback. Note that unlike prior work (Wing et al. 2016), here the advective feedback is calculated explicitly (indeed, all feedbacks are calculated online at every time step as the model is running). The budget residual is smaller than any other term through the first half of the simulation, though it approaches the magnitude of the longwave feedback by the end of the simulation. The advective feedback is dominated by the contribution from the column integrated horizontal advective flux of FMSE (not shown).

When cloud-radiative feedbacks are removed, the domain-mean var($\widehat{h}$) budget in the Zero-q_{cl}, q_{ci} ensemble has a smaller tendency in var($\widehat{h}$) and the longwave feedback, which here only has contributions from water vapor, is indistinguishable from zero (dashed lines in Figure 11a). The surface flux feedback is weaker until day 10, since it explicitly depends on wind speed and it takes longer fo the TC to form. Figure 11b shows the evolution of the longwave feedback in all simulations. Note that the longwave feedback is by definition zero in Fix-Rad, Fix-LW, and Homog-Rad. It is again apparent that removing cloud-radiative effects, specifically those due to ice clouds, effectively removes the longwave feedback. For example, the longwave feedback in Zero-q_{cl} is similar to that in CTRL, but in Zero-q_{ci} it is near zero. Removing longwave-water vapor interactions slightly reduces the longwave feedback, though this is a small effect compared

Accepted for publication in *Journal of the Atmospheric Sciences*. DOI 10.1175/JAS-D-21-0227.1.

to that due to clouds. These conclusions are unchanged if the var($\widehat{\mathrm{h}}$) budget is normalized by the domain-mean var($\widehat{\mathrm{h}}$) (see Figure S8 in the supplementary material).

The longwave cloud-radiative feedback contributes to both TC genesis and intensification. Figure 12 considers the composite mean of the longwave feedback over all times in which the TC has an intensity between 12-15 m s^{-1}. Compositing over times in which the TC has similar intensities removes any inherent dependence of the feedback on intensity. Simulations with all longwave cloud feedbacks removed (`Fix-Rad`, `Fix-LW`, `Homog-Rad`, `Zero-`$\mathrm{q_{cl}, q_{ci}}$) take longer to reach tropical storm strength (Figure 12a), emphasizing the importance of the longwave cloud feedback for the early stages of TC development. However, there is substantial spread in the value of the longwave feedback in the 12-15 m s^{-1} bin across simulations that reach tropical storm strength at similar times (around day 3), which indicates that the longwave feedback does not fully explain differences in the time to tropical storm strength across simulations. In particular, the longwave feedback in the `Zero-`$\mathrm{q_{ci}}$ simulation is near zero, but the ensemble mean time to tropical storm strength is only slightly delayed compared to simulations with a much stronger longwave feedback. However, I note that if those simulations whose longwave feedback is by definition zero (`Fix-Rad`, `Fix-LW`, `Homog-Rad`) are excluded, the correlation between the strength of the longwave feedback and the time to tropical storm strength persists and remains statistically significant ($r = -0.71$ across all simulations, $r = -0.78$ across the ensemble means). Similar results are obtained using other intensity bins below tropical storm strength (see Figures S9-S11 in the supplementary material).

Simulations with a stronger longwave feedback (at the same intensity) also have faster intensification rates, based on either the rate of change of V_{max} averaged between the time of first reaching tropical storm strength and the LMI (Figure 12b) or the number of days between first reaching tropical storm strength and reaching the LMI (Figure 12c). In both cases, there are high, statistically significant, correlation coefficients of $r = 0.98$ and $r = -0.80$, respectively, across the

Accepted for publication in *Journal of the Atmospheric Sciences*. DOI 10.1175/JAS-D-21-0227.1.

ensemble means. These correlations are not simply reflecting differences between intensification in simulations with and without the longwave feedback, but also across simulations with varying strengths of the longwave feedback. If those simulations whose longwave feedback is by definition zero (`Fix-Rad`, `Fix-LW`, `Homog-Rad`) are excluded, the correlations across the ensemble means between the longwave feedback and intensification rate, and time between tropical storm strength and LMI, are $r = 0.98$ and $r = -0.92$, respectively. Even if those simulations whose longwave feedback is near zero (`Zero-`q_{cl}, q_{ci}, `Zero-`q_{ci}) are additionally excluded, those correlations persist ($r = 0.92$ and $r = -0.94$). In some other bins, the correlations weaken below the threshold for statistical significance when simulations with zero and near-zero longwave feedbacks are removed (see Figures S9-S11 in the supplementary material). Overall, these results indicate that simulations with a stronger longwave feedback at a given intensity are able to intensify more quickly beyond that point. A similar, though weaker, relationship exists between the 12-15 m s^{-1} bin longwave feedback and the number of days between reaching hurricane strength and the LMI (Figure 12d), where I ignore simulations who never reach hurricane strength or who reach their LMI at the end of the simulation.

Unlike the longwave feedback, the strength of the surface flux feedback in the 12-15 m s^{-1} bin is not significantly correlated with the time it takes to reach tropical storm strength (Figure 13a). This is also true for other intensity bins below tropical storm strength (see Figures S12-S14 in the supplementary material). Note that while surface fluxes depend directly on TC intensity, the surface flux *feedback* may vary in magnitude across storms of similar intensities. This is because it depends not only on the magnitude of the surface fluxes, but their spatial structure and co-variability with $\widehat{h}$. The 12-15 m s^{-1} bin surface flux feedback is associated with greater intensification rates (Figure 13b,c,d), though the correlations are only statistically significant at the 95% level when considering all ensemble members across all simulations, not the ensemble means.

Accepted for publication in *Journal of the Atmospheric Sciences*. DOI 10.1175/JAS-D-21-0227.1.

The correlations are again weaker than that for the longwave feedback. Although the magnitude of the surface flux feedback in this intensity bin is typically larger than that of the longwave feedback, indicating that the surface flux feedback contributes strongly to TC development, the difference across simulations is more associated with the presence or absence of the longwave feedback, and to some extent, its strength.

Overall, my results indicate that stronger longwave feedbacks, contributed primarily by ice clouds, are associated with both faster development of a tropical storm as well as faster intensification after a tropical storm has formed. Relative to the strength of the surface flux feedback, the longwave feedback contributes most in the early stages of TC development.

5. Conclusions

Interactions between clouds, radiation, and circulations are fundamental to tropical climate, but until recently, the impact of these interactions on TCs has been relatively unexplored. In this study, I examined the role of radiative feedbacks in TC development using a suite of idealized convection-permitting simulations in which a TC is initialized from a warm, moist bubble. I performed five-member ensembles in which radiative feedbacks were removed in several different ways. In contrast to some prior work, I found that the presence or absence of diurnally varying insolation does not affect TC formation and intensification, *if the time-mean insolation is constrained to be the same*. However, I did find that radiative feedbacks resulting from spatially varying radiative heating significantly accelerate TC development. On its own, this result provides strong evidence for the relevance of radiative feedbacks to TCs. When combined with prior studies that have also considered the role of radiative feedbacks in spontaneous TC genesis, realistic case study simulations, and global climate models, it is clear that across a hierarchy of simulations, radiative feedbacks are critical for TC development.

Accepted for publication in *Journal of the Atmospheric Sciences*. DOI 10.1175/JAS-D-21-0227.1.

My results emphasize that the acceleration of TC development by radiative processes occurs due to feedbacks between horizontally and vertically varying radiative heating and the TC, not due to the mere presence or absence of radiative heating or cooling. Such radiative feedbacks have contributions from both longwave and shortwave processes and from variability in water vapor, liquid clouds, and ice clouds. I found that it is the longwave cloud radiative feedback that is responsible for the acceleration of TC development and ice clouds specifically are the biggest contributor to the differential radiative heating that drives the feedback. The ice clouds associated with deep convection provide a local anomalous warming of the lower-mid troposphere which enhances the TC's overturning circulation, including the low-level radial inflow, and shortens the time to approach saturation. My conclusion about the dominance of ice cloud radiative effects is supported by both the ensemble mechanism denial experiments and quantification of the feedbacks using the frozen moist static energy variance budget, since the longwave feedback diagnosed by the latter is near zero in the simulations in which ice clouds are transparent to radiation.

While the stark contrast in TC formation between simulations in which the longwave cloud radiative feedback is absent and in which it is present provides a clear demonstration that the existence of this feedback accelerates TC genesis, the results also suggest that, once formed, the TC's intensification rate is also related to the strength of the longwave feedback. The latter is true even across simulations in which the longwave feedback is present, but of varying magnitude. This indicates that the spatial distribution of ice clouds (as the biggest contributor to the longwave feedback) and their radiative effects may be an important factor in determining how quickly a TC intensifies. However, this conclusion must be considered within the context of the limitations of this study. While these simulations were designed to study TC formation from an initial disturbance in an idealized setting without complicating factors, some of the factors neglected, such as TC motion, background flow, and vertical wind shear, could influence the results. The five-member

Accepted for publication in *Journal of the Atmospheric Sciences*. DOI 10.1175/JAS-D-21-0227.1.

ensembles provide some measure of the stochastic nature of TC development, but may be under-dispersed. Finally, the use of a one-moment microphysics scheme surely impacts the quantitative details of the feedbacks studied here, compared to more advanced representations (e.g., Brown et al. 2016). However, given the fact that other studies using different models and different microphysics schemes have also indicated an acceleration of TC development by cloud-radiative feedbacks (e.g., Ruppert et al. 2020; Smith et al. 2020; Wu et al. 2021; Yang et al. 2021), this basic result is unlikely to be contingent on the specific microphysics scheme used here.

I also note the somewhat peculiar behavior of the Zero-q_{ci} simulation, in which the longwave feedback is essentially removed by making ice clouds transparent, but there is only a slight delay in the time to tropical storm formation compared to CTRL (though Zero-q_{ci} does exhibit a slower intensification rate). Why is Zero-q_{ci} able to form a TC much more quickly than Zero-q_{cl}, q_{ci}, despite the fact that both have near zero longwave feedbacks? It appears to be due to a combination of two factors: (1) Zero-q_{ci} has a somewhat greater var($\widehat{h}$) tendency than Zero-q_{cl}, q_{ci} because larger surface flux and shortwave feedbacks more than compensate for a slightly negative longwave feedback (Figure 6a, Figure S7); and (2) Zero-q_{ci} has a greater increase in V_{max} per unit increase in var($\widehat{h}$) (Figure 10d). The latter indicates that the var($\widehat{h}$) budget does not provide a complete picture of the processes that lead to TC development. Even within the context of the var($\widehat{h}$) budget, the longwave feedback is not the only factor that contributes and its quantification as $2\langle \widehat{h'} N'_L \rangle$ only reflects the direct longwave feedback, not indirect influences mediated by the circulation response.

Despite the aforementioned caveats, the implication of these results is that a good simulation of the spatial distribution of clouds (particularly ice clouds), their optical properties, and their radiative effects in forecast models may be important for accurately forecasting TC formation and intensification. Ice cloud-radiative feedbacks are present in forecast models and recent work has improved the representation of ice clouds in TC forecast models (e.g., Jin et al. 2014; Gopalakrishnan et al.

Accepted for publication in *Journal of the Atmospheric Sciences*. DOI 10.1175/JAS-D-21-0227.1.

2018; Heming et al. 2019; Bao et al. 2020). However, the role of ice clouds in radiative feedbacks, specifically, has not to date been a main focus of model improvement efforts in the context of TC prediction. Further improving the representation of ice clouds and their radiative effects in forecast models thus has the potential to yield critical advancements in TC forecasts. Some recent work has begun to evaluate cloud-radiative feedbacks in TC development using satellite observations (Wu et al. 2021), with results that are consistent with the simulations presented here, but there is more to be done to provide observational constraints on this important process, which will be a focus of my future work.

Acknowledgments. The author acknowledges helpful conversations with James H. Ruppert, Jr. and Daniel Chavas, and thanks three anonymous reviewers for their constructive feedback. This research was supported by funding from the NOAA Climate Program Office's Modeling, Analysis, Predictions, and Projections Program under Grant NA18OAR4310270, the National Science Foundation under Grant 1830724, NASA's New (Early Career) Investigator Program in Earth Science under Grant 80NSSC21K0932, and the Florida State University (FSU) Office of Research's First Year Assistant Professor (FYAP) program. The simulations were made possible by high-performance computing support from Cheyenne (doi:10.5065/D6RX99HX) provided by NCAR's Computational and Information Systems Laboratory, sponsored by the National Science Foundation. Additional computing was performed on the High Performance Computing (HPC) cluster at the Research Computing Center at FSU. The author also thanks Marat Khairoutdinov for providing and maintaining the System for Atmospheric Modeling (SAM) cloud-resolving model.

Data availability statement. The model input files used to run the simulations and post-processed model output data used to generate figures are publicly available in a github respository: `https://github.com/allison-wing/TCrad-bubble`.

Accepted for publication in *Journal of the Atmospheric Sciences*. DOI 10.1175/JAS-D-21-0227.1.

References

Bao, S., L. Bernardet, G. Thompson, E. Kalina, K. Newman, and M. Biswas, 2020: Impact of the hydrometeor vertical advection method on HWRF's simulated hurricane structure. *Wea. and Forecasting*, **35**, 723–737, doi:10.1175/WAF-D-19-0006.1.

Bretherton, C. S., P. N. Blossey, and M. Khairoutdinov, 2005: An energy-balance analysis of deep convective self-aggregation above uniform SST. *J. Atmos. Sci.*, **62**, 4273–4292.

Brown, B. R., M. M. Bell, and A. J. Frambach, 2016: Validation of simulated hurricane drop size distributions using polarimetric radar. *Geophys. Res. Let.*., **43**, 910–917, doi:10.1002/2015GL067278.

Bu, Y., R. Fovell, and K. Corbosiero, 2014: Influence of cloud radiative forcing on tropical cyclone structure. *J. Atmos. Sci.*, **71**, 1644–1662, doi:10.1175/JAS-D-13-0265.1.

Cangialosi, J. P., E. Blake, M. DeMaria, A. Penny, A. Latto, E. N. Rappaport, and V. Tallapragada, 2020: Recent progress in tropical cyclone intensity forecasting at the National Hurricane Center. *Wea. Forecasting*, **35**, 1913–1922, doi:10.1175/WAF-D-20-0059.1.

Carstens, J., and A. Wing, 2020: Tropical cyclogenesis from self-aggregated convection in numerical simulations of rotating radiative-convective equilibrium. *J. Adv. Model. Earth Syst.*, **12**, e2019MS002 020, doi:10.1029/2019MS002020.

Carstens, J. D., and A. A. Wing, 2022: A spectrum for convective self-aggregation based on background rotation. *J. Adv. Model. Earth Syst.*, doi:10.1029/2021MS002860.

Clough, S. A., M. W. Shephard, E. J. Mlawer, J. S. Delamere, M. J. Iacono, K. Cady-Pereira, S. Boukabara, and P. D. Brown, 2005: Atmospheric radiative transfer modeling: A summary of the AER codes. *J. Quant. Spectrosc. Radiat. Transfer*, **91**, 233–244.

Accepted for publication in *Journal of the Atmospheric Sciences*. DOI 10.1175/JAS-D-21-0227.1.

Craig, G., 1996: Numerical experiments on radiation and tropical cyclones. *Q. J. R. Meteorol. Soc.*, **122**, 415–422, doi:10.1002/qj.49712253006.

Davis, C. A., 2015: The formation of moist vortices and tropical cyclones in idealized simulations. *J. Atmos. Sci.*, **72**, 3499–3516, doi:10.1175/JAS-D-15-0027.1.

DeMaria, M., J. L. Franklin, M. J. Onderlinde, and J. Kaplan, 2021: Operational forecasting of tropical cyclone rapid intensification at the national hurricane center. *Atmosphere*, **12**, 683, doi:10.3390/atmos12060683.

DeMaria, M., C. Sampson, J. Knaff, and K. Musgrave, 2014: Is tropical cyclone intensity guidance improving? *Bull. Amer. Meteor. Soc.*, **95**, 387–398, doi:10.1175/BAMS-D-12-00240.1.

Ditchek, S. D., K. L. Corbosiero, R. G. Fovell, and J. Molinari, 2019a: Electrically active tropical cyclone diurnal pulses in the atlantic basin. *Mon. Wea. Rev.*, **147**, 3595–3607.

Ditchek, S. D., K. L. Corbosiero, R. G. Fovell, and J. Molinari, 2020: Electrically active diurnal pulses in Hurricane Harvey (2017). *Mon. Wea. Rev.*, **148**, 2283–2305.

Ditchek, S. D., J. Molinari, K. L. Corbosiero, and R. G. Fovell, 2019b: An objective climatology of tropical cyclone diurnal pulses in the atlantic basin. *Mon. Wea. Rev.*, **147**, 591–605.

Dunion, J., C. Thorncroft, and D. Nolan, 2019: Tropical cyclone diurnal cycle signals in a hurricane nature run. *Mon Wea. Rev.*, **147**, 363–388.

Dunion, J., C. Thorncroft, and C. Velden, 2014: The tropical cyclone diurnal cycle of mature hurricanes. *Mon. Weather Rev.*, **142**, 3900–3913.

Evans, R., and D. Nolan, 2019: Balanced and radiating wave responses to diurnal heating in trpoical cyclone-like vortices using a linear nonhdyrostatic model. *J. Atmos. Sci.*, **76**, 2575–2597.

Accepted for publication in *Journal of the Atmospheric Sciences*. DOI 10.1175/JAS-D-21-0227.1.

Fovell, R., Y. P. Bu, K. L. Corbosiero, W. Tung, Y. Cao, H.-C. Kuo, L. Hsu, and H. Su, 2016: Influence of cloud microphysics and radiation on tropical cyclone structure and motion. *Meteorological Monographs*, **56**, 11.1–11.27, doi:10.1175/AMSMONOGRAPHS-D-15-0006.1.

Fovell, R., K. L. Corbosiero, A. Seifert, and K.-N. Liou, 2010: Impact of cloud-radiative processes on hurricane track. *Geophys. Res. Lett.*, **37**, L07 808, doi:10.1029/2010GL042691.

Ge, X., Y. Ma, S. Zhou, and T. Li, 2014: Impacts of the diurnal cycle of radiation on tropical cyclone intensification and structure. *Advances in Atmospheric Sciences*, **31 (6)**, 1377–1385, doi:10.1007/s00376-014-4060-0.

Gopalakrishnan, S. G., and Coauthors, 2018: 2017 HFIP R&D activities summary: Recent results and operational implementation. Tech. Rep. HFIP2018-1, HFIP. URL https://hfip.org/documents/HFIP_AnnualReport_FY2017.pdf.

Gray, W., and R. Jacobson, 1977: Diurnal variation of deep cumulus convection. *Mon. Wea. Rev.*, **105**, 1171–1188.

Hakim, G., 2011: The mean state of axisymmetric hurricanes in statistical equilibrium. *J. Atmos. Sci.*, **68**, 1364–1376, doi:10.1175/2010JAS3644.1.

Held, I. M., R. S. Hemler, and V. Ramaswamy, 1993: Radiative-convective equilibrium with explicit two-dimensional moist convection. *Journal of the Atmospheric Sciences*, **50 (23)**, 3909–3927.

Heming, J., and Coauthors, 2019: Review of recent progress in tropical cyclone track forecasting and expression of uncertainties. *Tropical Cyclone Research and Review*, **8**, 181–218, doi:10.1016/j.tcrr.2020.01.001.

Accepted for publication in *Journal of the Atmospheric Sciences*. DOI 10.1175/JAS-D-21-0227.1.

Hill, K. A., and G. M. Lackmann, 2009a: Analysis of idealized tropical cyclone simulations using the Weather Research and Forecasting model: Sensitivity to turbulence parameterization and grid spacing. *Mon. Wea. Rev.*, **137**, 745–765, doi:10.1175/2008MWR2220.1.

Hill, K. A., and G. M. Lackmann, 2009b: Influence of environmental humidity on tropical cyclone size. *Mon. Wea. Rev.*, **137**, 3294–3315, doi:10.1175/2009MWR2679.1.

Hobgood, J. S., 1986: A possible mechanism for the diurnal oscillations of tropical cyclones. *J. Atmos. Sci.*, **43**, 2901–2922.

Iacono, M. J., J. S. Delamere, E. J. Mlawer, M. W. Shephard, S. A. Clough, and W. D. Collins, 2008: Radiative forcing by long-lived greenhousegases: calculations with the AER radiative transfer models. *J. Geophys. Res.*, **113**, D13 103, doi:10.1029/2008JD009944.

Jin, Y., and Coauthors, 2014: The impact of ice phase cloud parameterizations on tropical cyclone prediction. *Mon. Wea. Rev.*, **142**, 606–625, doi:10.1175/MWR-D-13-00058.1.

Khairoutdinov, M. F., and D. Randall, 2003: Cloud resolving modeling of the ARM Summer 1997 IOP: Model formulation, results, uncertainties, and sensitivities. *J. Atmos. Sci.*, **60**, 607–625.

Knaff, J., C. Slocum, and K. Musgrave, 2019: Quantification and exploration of diurnal oscillations in tropical cyclones. *Mon. Wea. Rev.*, **142**, 2105–2121.

Knutson, T., and Coauthors, 2020: Tropical cyclones and climate change assessment: Part II: Projected response to anthropogenic warming. *Bull. Amer. Meteor. Soc.*, **101**, E303–E322, doi: 10.1175/BAMS-D-18-0194.1.

Kossin, J., 2002: Daily hurricane variability inferred from GOES infrared imagery. *Mon. Weather Rev.*, **130**, 2260–2270.

Accepted for publication in *Journal of the Atmospheric Sciences*. DOI 10.1175/JAS-D-21-0227.1.

Melhauser, C., and F. Zhang, 2014: Diurnal radiation cycle impact on the pregenesis environment of Hurricane Karl (2010). *J. Atmos. Sci.*, **71**, 1242–1259, doi:10.1175/JAS-D-13-0116.1.

Mlawer, E. J., S. J. Taubman, P. D. Brown, M. J. Iacono, and S. A. Clough, 1997: Radiative transfer for inhomogeneous atmospheres: RRTM, a validated correlated-k model for the longwave. *J. Geophys. Res.*, **102**, 16 663–16 682.

Mol, W. B., C. C. van Heerwaarden, and L. Schlemmer, 2019: Surface moisture exchange under vanishing wind in simulations of idealized tropical convection. *Geophys. Res. Lett.*, **46**, 13 602–13 609, doi:10.1029/2019GL085047.

Morrison, H., J. A. Curry, and V. I. Khvorostyanov, 2005: A new double-moment microphysics parameterization for application in cloud and climate models. Part I: Description. *J. Atmos. Sci.*, **62**, 1665–1677, doi:10.1175/JAS3446.1.

Muller, C. J., and I. M. Held, 2012: Detailed investigation of the self-aggregation of convection in cloud-resolving simulations. *Journal of the Atmospheric Sciences*, **69 (8)**, 2551–2565, doi:10.1175/JAS-D-11-0257.1.

Muller, C. J., and D. M. Romps, 2018: Acceleration of tropical cyclogenesis by self-aggregation feedbacks. *Proceedings of the National Academy of Sciences*, doi:10.1073/pnas.1719967115.

Musgrave, K. D., R. K. Taft, J. L. Vigh, B. D. McNoldy, and W. H. Schubert, 2012: Time evolution of the intensity and size of tropical cyclones. *J. Adv. Model. Earth Syst.*, **4**, M08 001.

Naumann, A. K., B. Stevens, and C. Hohenegger, 2019: A moist conceptual model for the boundary layer structure and radiatively driven shallow circulations in the trades. *J. Atmos. Sci.*, **76**, 3129–3144, doi:10.1175/JAS-D-17-0030.1.

Accepted for publication in *Journal of the Atmospheric Sciences*. DOI 10.1175/JAS-D-21-0227.1.

Navarro, E., G. Hakin, and H. Willoughby, 2017: Balanced response of an axisymmetric tropical cyclone to periodic diurnal heating. *J. Atmos. Sci.*, **74**, 3325–3337.

Navarro, E. L., and G. J. Hakim, 2016: Idealized numerical modeling of the diurnal cycle of tropical cyclones. *J. Atmos. Sci.*, **73**, 4189–4201, doi:10.1175/JAS-D-15-0349.1.

Nicholls, M. E., 2015: An investigation of how radiation may cause accelerated rates of tropical cyclogenesis and diurnal cycles of convective activity. *Atmospheric Chemistry and Physics*, **15 (15)**, 9003–9029, doi:10.5194/acp-15-9003-2015.

O'Neill, M., D. Perez-Betancourt, and A. A. Wing, 2017: Accessible environments for diurnal-period waves in simulated tropical cyclones. *J. Atmos. Sci.*, **74**, 2489–2505, doi:10.1175/JAS-D-16-0294.1.

Rios-Berrios, R., 2020: Impacts of radiation and cold pools on the intensity and vortex tilt of weak tropical cyclones interacting with vertical wind shear. *J. Atmos. Sci.*, **77**, 669–689.

Ruppert, J., and M. O'Neill, 2019: Diurnal cloud and circulation changes in simulated tropical cyclones. *Geophys. Res. Lett.*, **46**, 502–511.

Ruppert, J., A. Wing, X. Tang, and E. Duran, 2020: The critical role of cloud-infrared radiation feedback in tropical cyclone development. *Proc. Nat. Acad. Sci.*, **117**, 27 884–27 892, doi:10.1073/pnas.2013584117.

Smith, W., M. E. Nicholls, and R. Pielke, 2020: The role of radiation in accelerating tropical cyclogenesis in idealized simulations. *J. Atmos. Sci.*, **77**, 1261–1277.

Stein, U., and P. Alpert, 1993: Factor separation in numerical simulations. *J. Atmos. Sci.*, **50**, 2107–2115.

Accepted for publication in *Journal of the Atmospheric Sciences*. DOI 10.1175/JAS-D-21-0227.1.

Tang, X., Z.-M. Tan, J. Fang, E. Munsell, and F. Zhang, 2019: Impact of the diurnal radiation contrast on the contraction of radius of maximum wind during intensification of Hurricane Edouard (2014). *J. Atmos. Sci.*, **76**, 421–432.

Tang, X., Z.-M. Tan, J. Fang, Y. Sun, and F. Zhang, 2017: Impact of the diurnal radiation cycle on secondary eyewall formation. *J. Atmos. Sci.*, **74**, 3079–3098.

Tang, X., and F. Zhang, 2016: Impacts of the diurnal radiation cycle on the formation, intensity, and structure of hurricane edouard (2014). *Journal of the Atmospheric Sciences*, **73 (7)**, 2871–2892, doi:10.1175/JAS-D-15-0283.1.

Thompson, G., P. R. Field, R. M. Rasmussen, and W. D. Hall, 2008: Explicit forecasts of winter precipitation using an improved bulk microphysics scheme. Part II: Implementation of a new snow parameterization. *Mon. Wea. Rev.*, **136**, 5095–5115, doi:10.1175/2008MWR2387.1.

Trabing, B., M. Bell, and B. Brown, 2019: Impacts of radiation and upper-tropospheric temperatures on tropical cyclone structure and intensity. *J. Atmos. Sci.*

Trabing, B. C., and M. M. Bell, 2020: Understanding error distributions of hurricane intensity forecasts during rapid intensity changes. *Weather and Forecasting*, **35**, 2219–2234, doi:10.1175/WAF-D-19-0253.1.

Trabing, B. C., and M. M. Bell, 2021: The sensitivity of eyewall replacement cycles to shortwave radiation. *J. Geophys. Res.*, **126**, e2020JD034 016, doi:10.1029/2020JD034016.

Vigh, J. L., and W. H. Schubert, 2009: Rapid development of the tropical cyclone warm core. *J. Atmos. Sci.*, **66**, 3350.

Waliser, D. E., and Coauthors, 2009: Cloud ice: A climate model challenge with signs and expectations of progress. *J. Geophys. Res.*, **114**, D00A21, doi:10.1029/2008JD010015.

Accepted for publication in *Journal of the Atmospheric Sciences*. DOI 10.1175/JAS-D-21-0227.1.

Wing, A., and Coauthors, 2019: Moist static energy budget analysis of tropical cyclone intensification in high-resolution climate models. *J. Climate*, **32**, 6071–6095, doi:10.1175/JCLI-D-18-0599.1.

Wing, A., and Coauthors, 2020: Clouds and convective self-aggregation in a multi-model ensemble of radiative-convective equilibrium simulations. *J. Adv. Model. Earth Syst.*, **12**, e2020MS002 138, doi:10.1029/2020MS002138.

Wing, A. A., S. J. Camargo, and A. H. Sobel, 2016: Role of radiative-convective feedbacks in spontaneous tropical cyclogenesis in idealized numerical simulations. *Journal of the Atmospheric Sciences*, **73**, 2633–2642, doi:10.1175/JAS-D-15-0380.1.

Wing, A. A., K. Emanuel, C. E. Holloway, and C. Muller, 2017: Convective self-aggregation in numerical simulations: A review. *Surveys in Geophysics*, **38 (6)**, 1173–1197, doi:10.1007/s10712-017-9408-4.

Wing, A. A., and K. A. Emanuel, 2014: Physical mechanisms controlling self-aggregation of convection in idealized numerical modeling simulations. *J. Adv. Model. Earth Syst.*, **6**, 59–74, doi:10.1002/2013MS000269.

Wing, A. A., K. A. Reed, M. Satoh, B. Stevens, S. Bony, and T. Ohno, 2018: Radiative-Convective Equilibrium Model Intercomparison Project. *Geosci. Model Dev.*, **11**, 793–813, doi:10.5194/gmd-11-793-2018.

Wu, Q., J. Hong, and Z. Ruan, 2020: Diurnal variations in tropical cyclone intensification. *Geophys. Res. Lett.*, **47**, e2020GL090 397, doi:10.1029/2020GL090397.

Wu, Q., and Z. Ruan, 2016: Diurnal variations of the areas and temperatures in tropical cyclone clouds. *Q. J. R. Meteorol. Soc.*, **142**, 2788–2796, doi:10.1002/qj.2868.

Accepted for publication in *Journal of the Atmospheric Sciences*. DOI 10.1175/JAS-D-21-0227.1.

Wu, S.-N., B. J. Soden, and D. S. Nolan, 2021: Examining the role of cloud radiative interactions in tropical cyclone development using satellite measurements and WRF simulations. *Geophys. Res. Let..*, **48**, e2021GL093 259, doi:10.1029/2021GL093259.

Yang, B., J. Nie, and Z.-M. Tan, 2021: Radiation feedback accellerates the formation of Typhoon Haiyan (2013): The critical role of mid-level circulation. *Geophys. Res. Lett.*, **48**, e2021GL094 168, doi:10.1029/2021GL094168.

Yang, B., and Z.-M. Tan, 2020: Interactive radiation accelerates the intensification of the midlevel vortex for tropical cyclogenesis. *J. Atmos. Sci.*, **77**, 4051–4065, doi:10.1175/JAS-D-20-0094.1.

Zhang, B., B. J. Soden, G. A. Vecchi, and W. Yang, 2021: The role of radiative interactions in tropical cyclone development under realistic boundary conditions. *J. Climate*, **34**, 2079–2091, doi:10.1175/JCLI-D-20-0574.1.

Zhang, F., and J. A. Sippel, 2009: Effects of moist convection on hurricane predictability. *J. Atmos. Sci.*, **66**, 1944–1961, doi:10.1175/2009JAS2824.1.

Zhang, J., J. Dunion, and D. Nolan, 2020: In situ observations of the diurnal variation in the boundary layer of mature hurricanes. *Geophys. Res. Lett.*, **47**, 1–8.

Zhou, S., Y. Ma, and X. Ge, 2016: Impacts of the diurnal cycle of solar radiation on spiral rainbands. *Advances in Atmospheric Sciences*, **33 (9)**, 1085–1095, doi:10.1007/s00376-016-5229-5.

Accepted for publication in *Journal of the Atmospheric Sciences*. DOI 10.1175/JAS-D-21-0227.1.

LIST OF TABLES

Table 1. Simulations 39

Table 2. Statistics for evolution of maximum azimuthal-mean tangential wind, calculated based on time series smoothed by the 6-hour running mean. Ensemble mean is the number provided first, ensemble range is provided in parentheses, all in units of days. Statistical significance is indicated by bold font, based on when the 95% confidence interval for the difference in the mean from CTRL does not include zero. 40

Accepted for publication in *Journal of the Atmospheric Sciences*. DOI 10.1175/JAS-D-21-0227.1.

TABLE 1. Simulations

Simulation	Change to Radiation	Feedbacks Removed	Feedbacks Present
CTRL	None	None	LW-all, SW-all
No-Diurnal	Constant insolation	Diurnal Insolation	LW-all, SW-all
Homog-Rad	Tendency spatially homogenized at each level	LW-all, SW-all	None
Fix-Rad	Externally prescribed LW & SW tendency	LW-all, SW-all	None
Fix-LW	Externally prescribed LW tendency	LW-all	SW-all
Fix-SW	Externally prescribed SW tendency	SW-all	LW-all
Fix-q_v	Prescribed water vapor in LW & SW	LW- & SW-water vapor	Cloud
Fix-LW-q_v	Prescribed water vapor in LW	LW-water vapor	SW-water vapor, Cloud
Fix-SW-q_v	Prescribed water vapor in SW	SW-water vapor	LW-water vapor, Cloud
Zero-q_{cl}, q_{ci}	Zeroed clouds in LW & SW	Liquid & ice cloud	Water vapor
Zero-q_{cl}	Zeroed liquid clouds in LW & SW	Liquid cloud	Water vapor, ice cloud
Zero-q_{ci}	Zeroed ice clouds in LW & SW	Ice cloud	Water vapor, liquid cloud

Accepted for publication in *Journal of the Atmospheric Sciences*. DOI 10.1175/JAS-D-21-0227.1.

TABLE 2. Statistics for evolution of maximum azimuthal-mean tangential wind, calculated based on time series smoothed by the 6-hour running mean. Ensemble mean is the number provided first, ensemble range is provided in parentheses, all in units of days. Statistical significance is indicated by bold font, based on when the 95% confidence interval for the difference in the mean from CTRL does not include zero.

Simulation	Days to 18 m s^{-1}	Days to 33 m s^{-1}	Days to LMI
	Mean (Range)	Mean (Range)	Mean (Range)
CTRL	3.23 (0.38)	3.72 (0.29)	5.02 (0.67)
No-Diurnal	3.08 (0.29)	3.62 (0.38)	4.96 (0.54)
Homog-Rad	**6.28** (1.92)	**7.63** (2.96)	**9.37** (1.21)
Fix-Rad	**6.92** (2.00)	**8.51** (1.63)	**9.63** (0.88)
Fix-LW	**7.39** (1.13)	**9.00** (1.46)	**9.98** (0.04)
Fix-SW	**2.97** (0.54)	3.57 (0.42)	**4.40** (0.33)
Fix-q_v	**2.85** (0.38)	**3.42** (0.67)	**4.58** (0.72)
Fix-LW-q_v	**2.90** (0.46)	**3.45** (0.50)	4.93 (0.79)
Fix-SW-q_v	3.10 (0.63)	3.72 (0.46)	5.04 (0.79)
Zero-q_{cl}, q_{ci}	**5.13** (1.00)	**6.19** (0.92)	**8.21** (1.42)
Zero-q_{cl}	3.24 (0.33)	3.76 (0.21)	5.19 (0.54)
Zero-q_{ci}	**3.71** (1.08)	**4.34** (1.17)	**8.13** (3.38)

Accepted for publication in *Journal of the Atmospheric Sciences*. DOI 10.1175/JAS-D-21-0227.1.

LIST OF FIGURES

Fig. 1. Water vapor (colors) and temperature (black lines) perturbations in the bubble from which the simulations are initialized. The temperature contours are every 1 K, with the center contour T' = 10 K. (a) shows a horizontal section at a height of 4 km and (b) shows a vertical cross section through the center of the domain in y. 44

Fig. 2. (a) Radiative heating rate profiles prescribed in the `Fix-Rad` (black), `Fix-LW` (blue), and `Fix-SW` (red) simulations. Note that in `Fix-LW` the shortwave heating is calculated interactively, and in `Fix-SW` the longwave heating is calculated interactively. (b) Water vapor mixing ratio profile prescribed in the radiative transfer calculation in the Fix-q_v, Fix-LW-q_v, and Fix-SW-q_v simulations. Note that in Fix-LW-q_v, the simulated water vapor profile is used in the shortwave radiative transfer calculation, and in Fix-SW-q_v the simulated water vapor profile is used in the longwave radiative transfer calculation. 45

Fig. 3. Evolution of maximum near-surface azimuthal mean tangential wind compared to `CTRL` in (a) `No-Diurnal`, (b) `Homog-Rad`, and (c) `Fix-Rad`. The thick line is the ensemble mean of each set of simulations. 46

Fig. 4. Hourly-averaged outgoing longwave radiation (OLR; Wm^{-2}; panels a-e and k-o) and precipitable water (PW; mm; panels f-j and p-t) in the `CTRL` (left panels) and `Homog-Rad` (right panels) simulations. Ensemble member one is shown for each. The day 1 panel shows the average between 24 and 25 hours from the beginning of the simulation, which is at local noon (the time of maximum insolation), and similarly for days 2, 3, 4, and 5. 47

Fig. 5. Evolution of maximum near-surface azimuthal mean tangential wind compared to `CTRL` in the ensembles with (a) fixed radiation, (b) fixed water vapor, and (c) zeroed clouds. The thick line is the ensemble mean of each set of simulations. 48

Fig. 6. (a) Azimuthal mean net column shortwave flux convergence (N_S) and (b) azimuthal mean net column longwave flux convergence (N_L), averaged over days 3-4, in `CTRL` (solid black), Fix-q_v (dashed gray), Zero-q_{cl},q_{ci} (solid gray), Zero-q_{ci} (solid blue), and Zero-q_{cl} (solid green). The azimuthal mean clear-sky (CS) net column flux convergence in `CTRL` is shown in the thin black dash-dot line. The ensemble mean of each set of simulations is plotted, with the error bars indicating the ensemble range. Note the different y-axis scale in (a) and (b). 49

Fig. 7. Anomaly of azimuthal mean longwave radiative heating rate from its radius-weighted mean (K d^{-1}; color shading), radius of maximum azimuthal mean tangential wind (black line), and contours of ice cloud condensate (cyan) and liquid cloud condensate (green), plotted as a function of height and radius from the tracked TC center for `CTRL` (first column; a-e), Zero-q_{cl},q_{ci} (second column; f-j), Zero-q_{ci} (third column; k-o), Zero-q_{cl} (fourth column; p-t). The data are daily averages centered at local noon (time of maximum insolation); i.e., the day 1 average (first row) is the average from hours 12-36 of the simulation. The cloud condensate contours are 0.01 g kg^{-1} (thin lines) and 0.1 g kg^{-1} (thick lines) and longwave heating rate anomaly contours are every 1 K d^{-1}. The radius-weighted mean is taken over all radii, but only the innermost 600 km is shown. Ensemble member 1 is shown. 50

Fig. 8. The left column shows the temporal evolution of the azimuthal mean radial wind (m s^{-1}) at z = 194 m (third model level), as a function of radius in the color shading. The black line indicates the radius of maximum azimuthal mean tangential wind at the lowest model level. The right column shows the temporal evolution of azimuthal mean relative humidity (computed over liquid at temperatures above freezing and over ice at temperatures below

Accepted for publication in *Journal of the Atmospheric Sciences*. DOI 10.1175/JAS-D-21-0227.1.

freezing, following SAM's thermodynamics) averaged over radii from 0 to 100 km, as a function of height. In both, ensemble member 1 of the (first row: a,e) CTRL, (second row: b,f) Zero-q_{cl},q_{ci}, (third row: c,g) Zero-q_{ci}, and (fourth row: d,h) Zero-q_{cl} simulations is displayed. The colorbar in the left column saturates at 0; only variability in inward radial winds is displayed. The adjustment to the initialization within approximately the first half day of simulation can be seen in the relative humidity plots. 51

Fig. 9. Anomaly of azimuthal mean longwave radiative heating rate from its radius-weighted mean (K d^{-1}; color shading) plotted as a function of height and radius from the tracked TC center for CTRL (first column; a-e), linear sum of ice and liquid cloud (second column; f-j), and non-linear interaction (third column; k-o). The radius of maximum azimuthal mean tangential wind (black line) and contours of ice cloud condensate (cyan) and liquid cloud condensate (green) in CTRL are shown in each panel for reference. The data are daily averages centered at local noon (time of maximum insolation); i.e., the day 1 average (first row) is the average from hours 12-36 of the simulation. The cloud condensate contours are 0.01 g kg^{-1} (thin lines) and 0.1 g kg^{-1} (thick lines) and longwave heating rate anomaly contours are every 1 K d^{-1}. The radius-weighted mean is taken over all radii, but only the innermost 600 km is shown. Ensemble member 1 is shown. 52

Fig. 10. Relationship between the domain-mean spatial variance of column-integrated frozen moist static energy (var($\widehat{h}$);J^{2}m^{-4}) and the maximum azimuthal mean tangential wind. Hourly values of each are plotted from the start of the simulation up until the time of the TC's lifetime maximum intensity. The legend indicates the correlation coefficients; all are statistically significant at least at the 95% confidence level. Ensemble member 1 is shown for each. . . . 53

Fig. 11. (a) Daily mean, domain-mean var($\widehat{h}$) budget for CTRL (solid lines) and Zero-q_{cl},q_{ci} (dashed lines), including contributions to the var($\widehat{h}$) tendency from the longwave ($2\langle\widehat{h}'N_L'\rangle$; blue), shortwave ($2\langle\widehat{h}'N_S'\rangle$; red), surface flux ($2\langle\widehat{h}'F_K'\rangle$; green), and advective feedbacks ($-2\langle\widehat{h}'\nabla_h\cdot\widehat{\mathbf{u}h}\rangle$; pink). The variance tendency ($d$var$(\widehat{h})/dt$; black) and the budget residual (gray) are also shown. (b) Daily mean longwave feedback, $2\langle\widehat{h}'N_L'\rangle$, in all simulations. Note that $2\langle\widehat{h}'N_L'\rangle$ is by definition zero in Fix-Rad, Fix-LW, and Homog-Rad. In both (a) and (b), the solid line shows the ensemble mean and the error bars show the ensemble range. Hourly means are noisier but have similar dependencies (not shown). 54

Fig. 12. Composite mean of the longwave feedback, $2\langle\widehat{h}'N_L'\rangle$, over times at which V_{max} is between 12-15 m s^{-1}, against (a) the time to reach tropical storm strength (18 m s^{-1}), (b) the average intensification rate (m s^{-1}d^{-1}) between the time of tropical storm strength and the lifetime maximum intensity (LMI), (c) the time to intensify from tropical storm strength to the LMI, and (c) the time to intensify from hurricane strength (33 m s^{-1}) to the LMI. A six-hour running mean is applied to V_{max} before computing the statistics. Note that $2\langle\widehat{h}'N_L'\rangle$ is by definition zero in Fix-Rad, Fix-LW, and Homog-Rad. The correlation coefficient is indicated across all simulations (r; small symbols) and across the ensemble means (r_{em}; large bold symbols); similar results are found when considering an individual ensemble member. All correlations are statistically significant at the 99% level except (d) for the ensemble mean, which is significant at the 90% level. 55

Fig. 13. Composite mean of the surface flux feedback, $2\langle\widehat{h}'F_K'\rangle$, over times at which V_{max} is between 12-12 m s^{-1}, against (a) the time to reach tropical storm strength (18 m s^{-1}), (b) the average intensification rate (m s^{-1}d^{-1}) b5tween the time of tropical storm strength and the lifetime maximum intensity (LMI), (c) the time to intensify from tropical storm strength to the LMI, and (c) the time to intensify from hurricane strength (33 m s^{-1}) to the LMI. A six-hour

running mean is applied to V_{max} before computing the statistics. The correlation coefficient is indicated across all simulations (r; small symbols) and across the ensemble means (r_{em}; large bold symbols); similar results are found when considering an individual ensemble member. The correlations across all simulations are all statistically significant at the 95% level, while none of the correlations across the ensemble means are (except for (d), which is significant at the 90% level). 56

Accepted for publication in *Journal of the Atmospheric Sciences*. DOI 10.1175/JAS-D-21-0227.1.

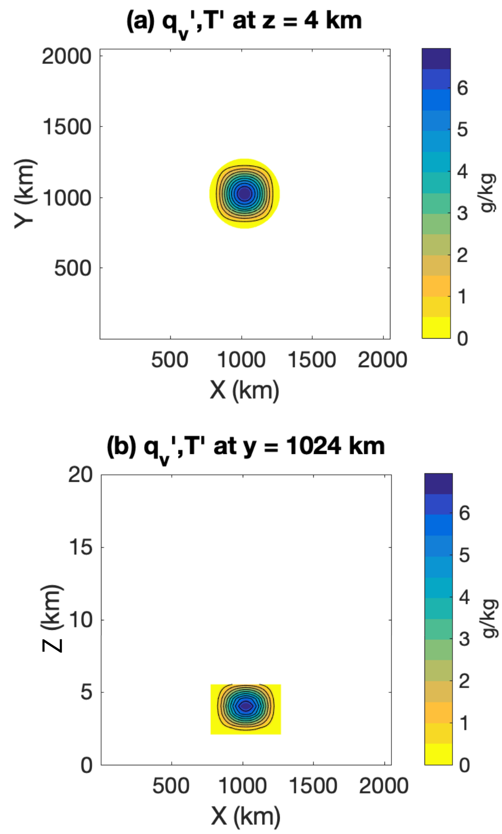

FIG. 1. Water vapor (colors) and temperature (black lines) perturbations in the bubble from which the simulations are initialized. The temperature contours are every 1 K, with the center contour T' = 10 K. (a) shows a horizontal section at a height of 4 km and (b) shows a vertical cross section through the center of the domain in y.

Accepted for publication in *Journal of the Atmospheric Sciences*. DOI 10.1175/JAS-D-21-0227.1.

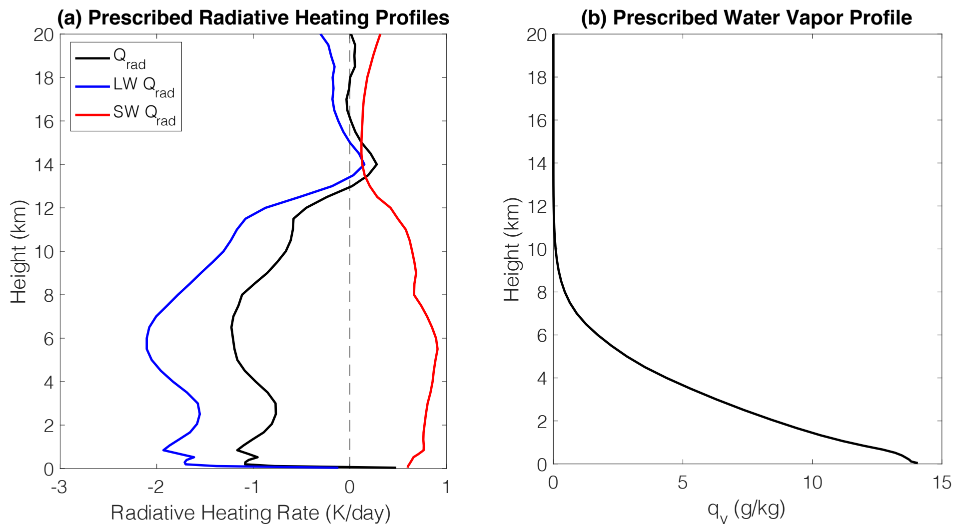

FIG. 2. (a) Radiative heating rate profiles prescribed in the `Fix-Rad` (black), `Fix-LW` (blue), and `Fix-SW` (red) simulations. Note that in `Fix-LW` the shortwave heating is calculated interactively, and in `Fix-SW` the longwave heating is calculated interactively. (b) Water vapor mixing ratio profile prescribed in the radiative transfer calculation in the Fix-q_v, Fix-LW-q_v, and Fix-SW-q_v simulations. Note that in Fix-LW-q_v, the simulated water vapor profile is used in the shortwave radiative transfer calculation, and in Fix-SW-q_v the simulated water vapor profile is used in the longwave radiative transfer calculation.

Accepted for publication in *Journal of the Atmospheric Sciences*. DOI 10.1175/JAS-D-21-0227.1.

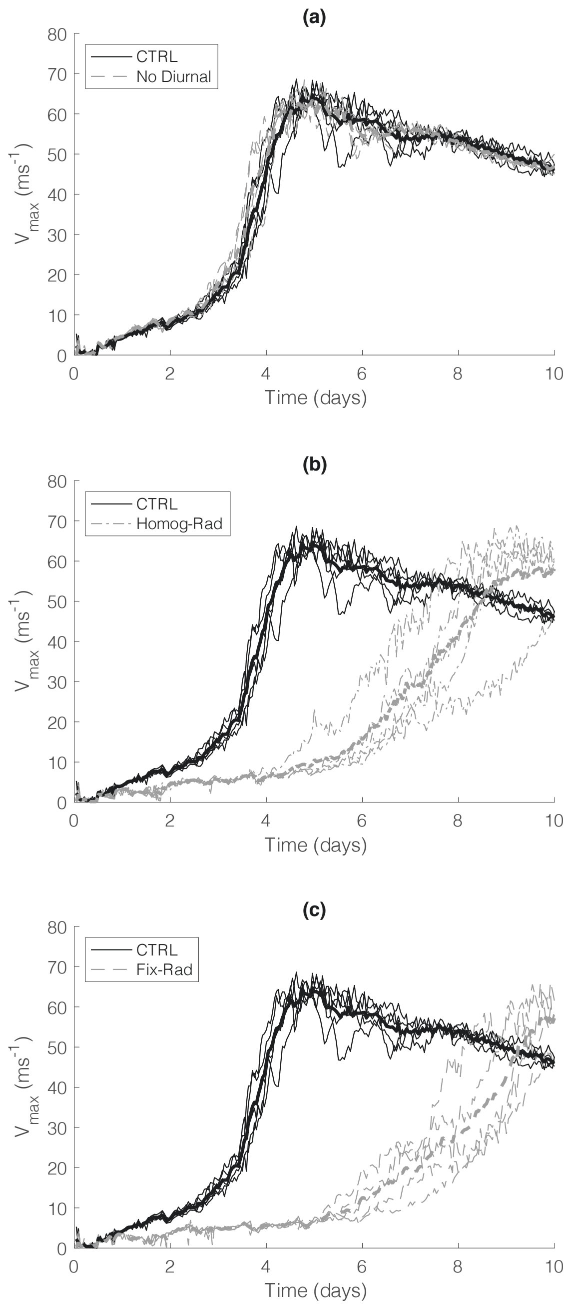

FIG. 3. Evolution of maximum near-surface azimuthal mean tangential wind compared to `CTRL` in (a) `No-Diurnal`, (b) `Homog-Rad`, and (c) `Fix-Rad`. The thick line is the ensemble mean of each set of simulations.

Accepted for publication in *Journal of the Atmospheric Sciences.* DOI 10.1175/JAS-D-21-0227.1.

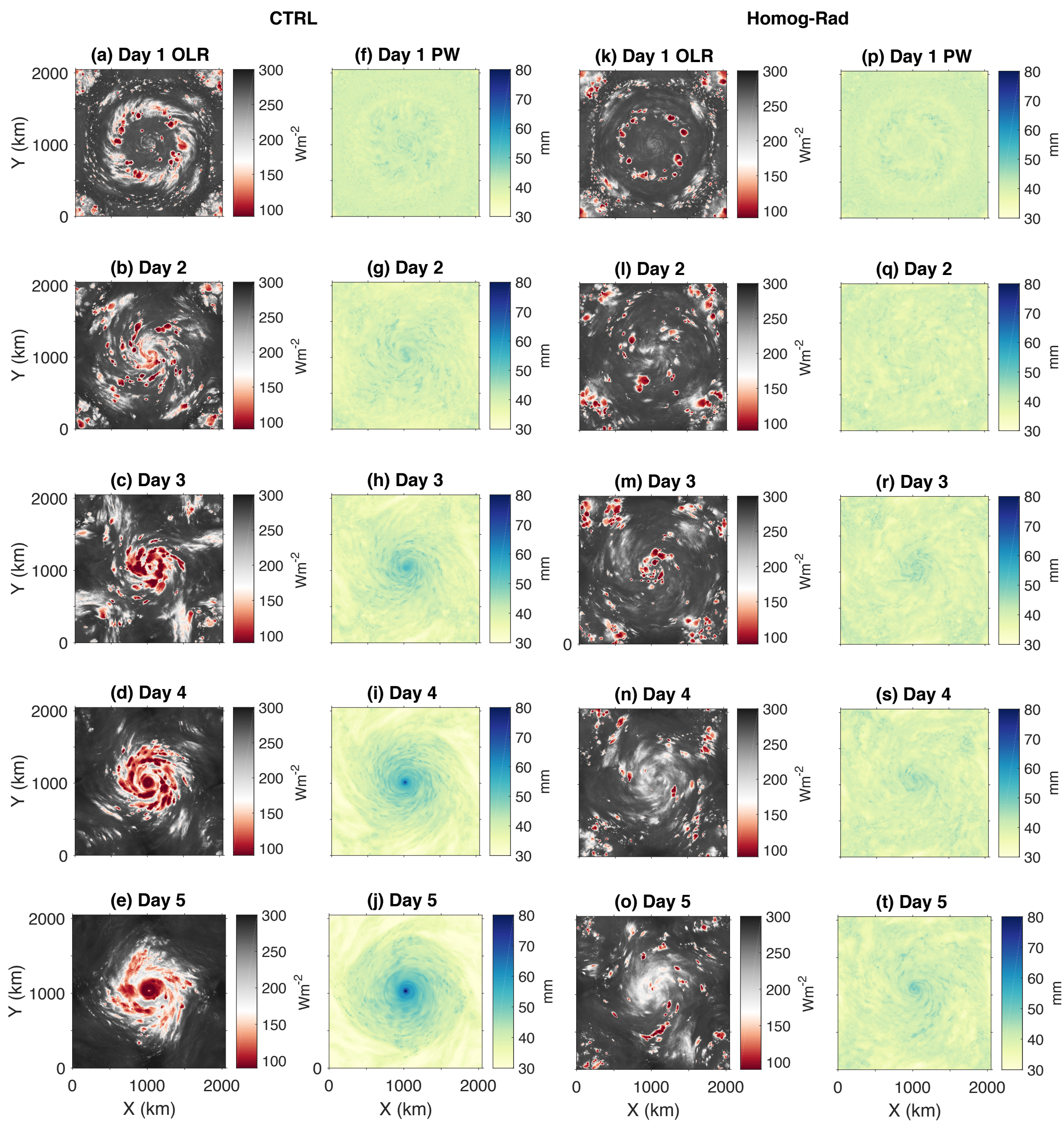

FIG. 4. Hourly-averaged outgoing longwave radiation (OLR; Wm^{-2}; panels a-e and k-o) and precipitable water (PW; mm; panels f-j and p-t) in the `CTRL` (left panels) and `Homog-Rad` (right panels) simulations. Ensemble member one is shown for each. The day 1 panel shows the average between 24 and 25 hours from the beginning of the simulation, which is at local noon (the time of maximum insolation), and similarly for days 2, 3, 4, and 5.

Accepted for publication in *Journal of the Atmospheric Sciences*. DOI 10.1175/JAS-D-21-0227.1.

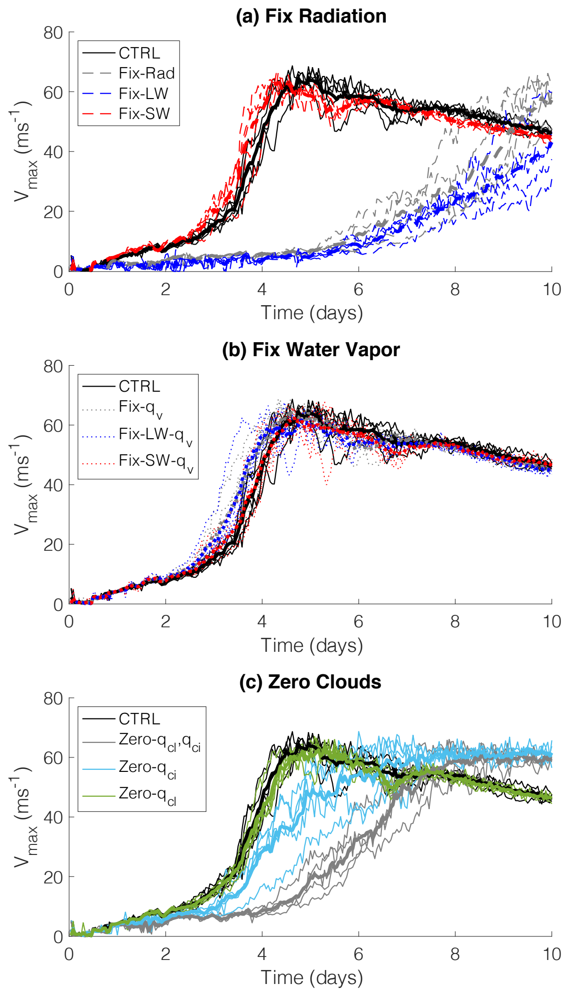

FIG. 5. Evolution of maximum near-surface azimuthal mean tangential wind compared to CTRL in the ensembles with (a) fixed radiation, (b) fixed water vapor, and (c) zeroed clouds. The thick line is the ensemble mean of each set of simulations.

Accepted for publication in *Journal of the Atmospheric Sciences*. DOI 10.1175/JAS-D-21-0227.1.

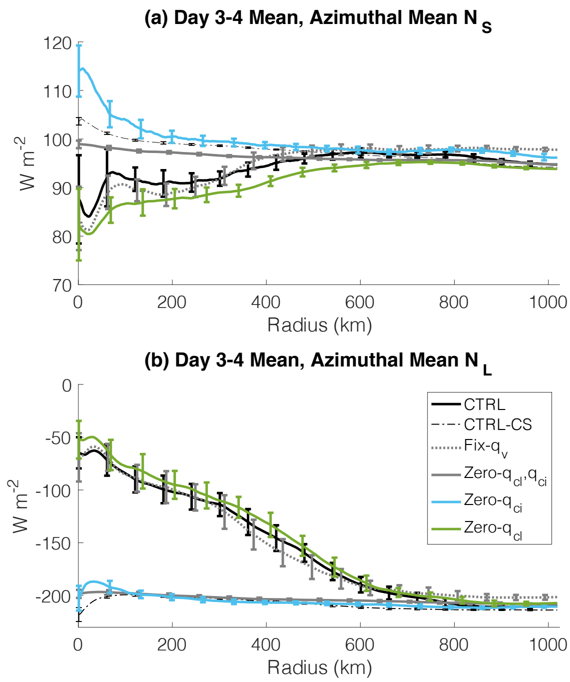

FIG. 6. (a) Azimuthal mean net column shortwave flux convergence (N_S) and (b) azimuthal mean net column longwave flux convergence (N_L), averaged over days 3-4, in CTRL (solid black), Fix-q_v (dashed gray), Zero-q_{cl},q_{ci} (solid gray), Zero-q_{ci} (solid blue), and Zero-q_{cl} (solid green). The azimuthal mean clear-sky (CS) net column flux convergence in CTRL is shown in the thin black dash-dot line. The ensemble mean of each set of simulations is plotted, with the error bars indicating the ensemble range. Note the different y-axis scale in (a) and (b).

Accepted for publication in *Journal of the Atmospheric Sciences*. DOI 10.1175/JAS-D-21-0227.1.

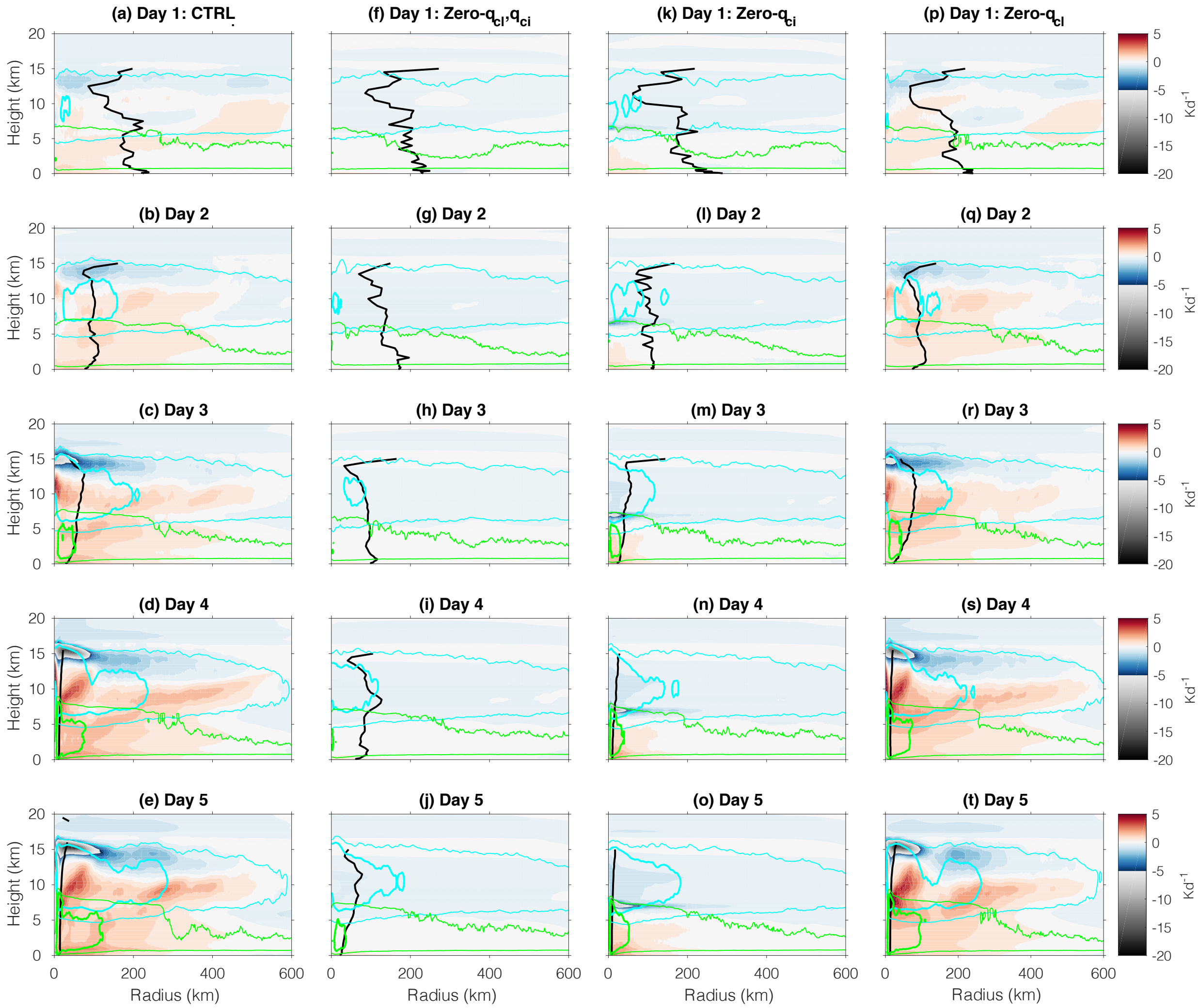

FIG. 7. Anomaly of azimuthal mean longwave radiative heating rate from its radius-weighted mean (K d^{-1}; color shading), radius of maximum azimuthal mean tangential wind (black line), and contours of ice cloud condensate (cyan) and liquid cloud condensate (green), plotted as a function of height and radius from the tracked TC center for CTRL (first column; a-e), Zero-q_{cl},q_{ci} (second column; f-j), Zero-q_{ci} (third column; k-o), Zero-q_{cl} (fourth column; p-t). The data are daily averages centered at local noon (time of maximum insolation); i.e., the day 1 average (first row) is the average from hours 12-36 of the simulation. The cloud condensate contours are 0.01 g kg^{-1} (thin lines) and 0.1 g kg^{-1} (thick lines) and longwave heating rate anomaly contours are every 1 K d^{-1}. The radius-weighted mean is taken over all radii, but only the innermost 600 km is shown. Ensemble member 1 is shown.

Accepted for publication in *Journal of the Atmospheric Sciences*. DOI 10.1175/JAS-D-21-0227.1.

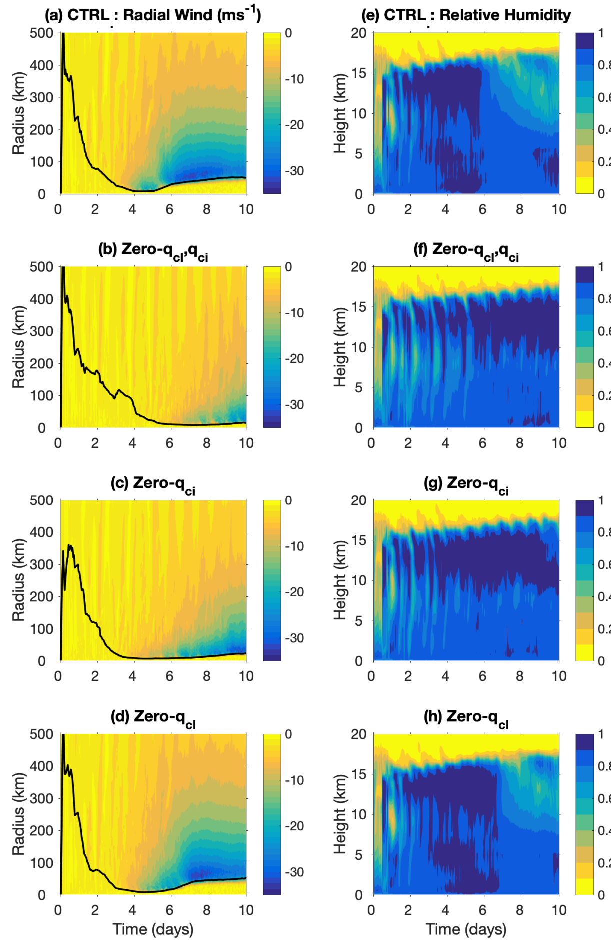

FIG. 8. The left column shows the temporal evolution of the azimuthal mean radial wind (m s^{-1}) at z = 194 m (third model level), as a function of radius in the color shading. The black line indicates the radius of maximum azimuthal mean tangential wind at the lowest model level. The right column shows the temporal evolution of azimuthal mean relative humidity (computed over liquid at temperatures above freezing and over ice at temperatures below freezing, following SAM's thermodynamics) averaged over radii from 0 to 100 km, as a function of height. In both, ensemble member 1 of the (first row: a,e) CTRL, (second row: b,f) Zero-q_{cl},q_{ci}, (third row: c,g) Zero-q_{ci}, and (fourth row: d,h) Zero-q_{cl} simulations is displayed. The colorbar in the left column saturates at 0; only variability in inward radial winds is displayed. The adjustment to the initialization within approximately the first half day of simulation can be seen in the relative humidity plots.

Accepted for publication in *Journal of the Atmospheric Sciences*. DOI 10.1175/JAS-D-21-0227.1.

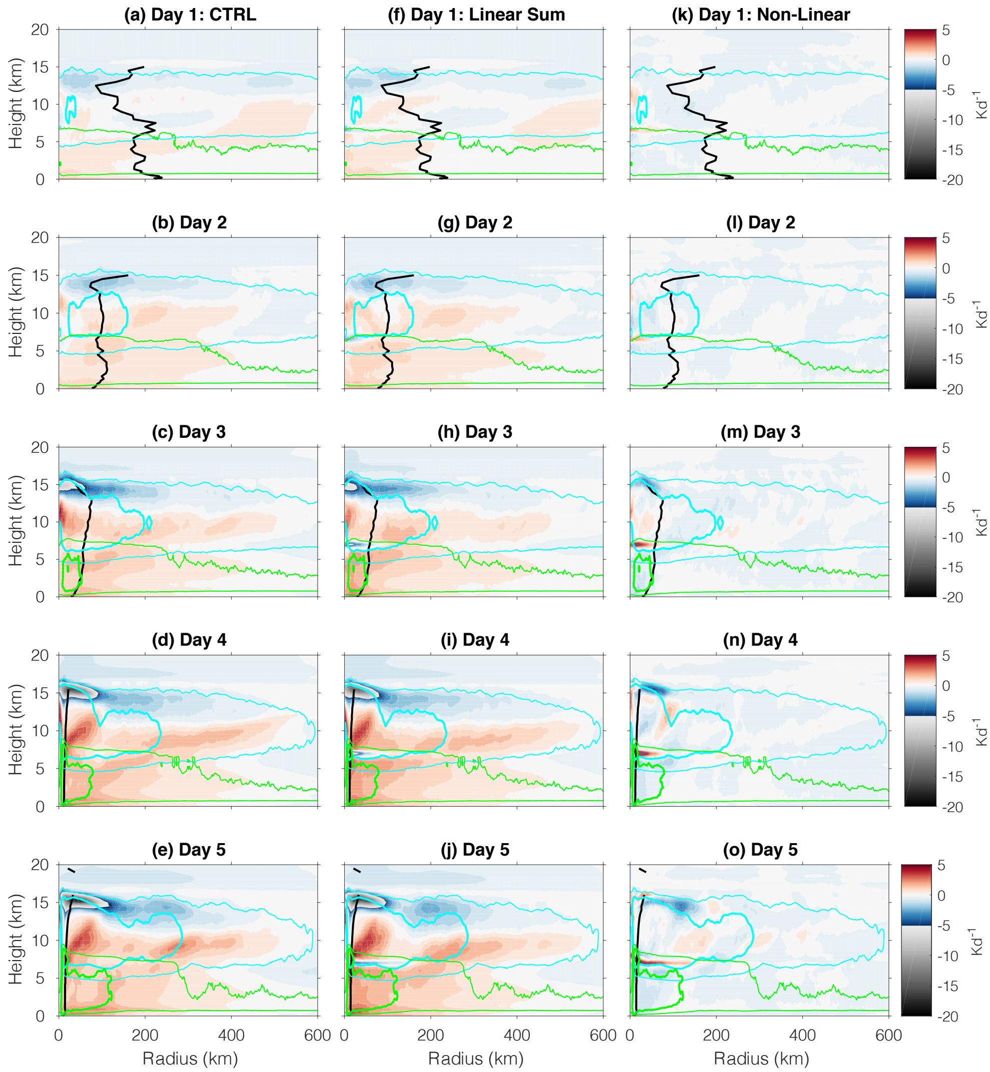

FIG. 9. Anomaly of azimuthal mean longwave radiative heating rate from its radius-weighted mean (K d^{-1}; color shading) plotted as a function of height and radius from the tracked TC center for CTRL (first column; a-e), linear sum of ice and liquid cloud (second column; f-j), and non-linear interaction (third column; k-o). The radius of maximum azimuthal mean tangential wind (black line) and contours of ice cloud condensate (cyan) and liquid cloud condensate (green) in CTRL are shown in each panel for reference. The data are daily averages centered at local noon (time of maximum insolation); i.e., the day 1 average (first row) is the average from hours 12-36 of the simulation. The cloud condensate contours are 0.01 g kg^{-1} (thin lines) and 0.1 g kg^{-1} (thick lines) and longwave heating rate anomaly contours are every 1 K d^{-1}. The radius-weighted mean is taken over all radii, but only the innermost 600 km is shown. Ensemble member 1 is shown.

Accepted for publication in *Journal of the Atmospheric Sciences*. DOI 10.1175/JAS-D-21-0227.1.

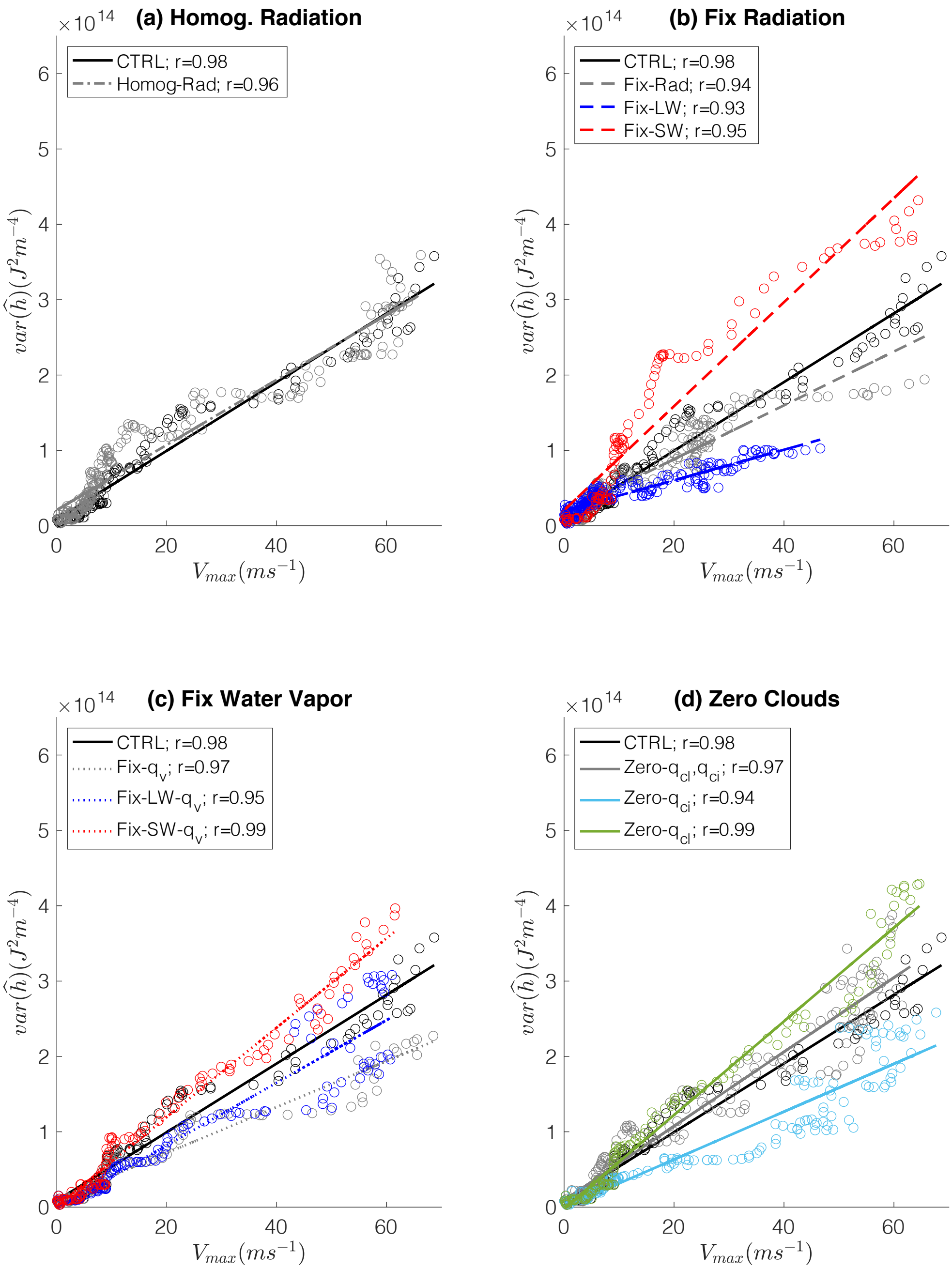

FIG. 10. Relationship between the domain-mean spatial variance of column-integrated frozen moist static energy ($\mathrm{var}(\widehat{\mathrm{h}}); \mathrm{J}^2\mathrm{m}^{-4}$) and the maximum azimuthal mean tangential wind. Hourly values of each are plotted from the start of the simulation up until the time of the TC's lifetime maximum intensity. The legend indicates the correlation coefficients; all are statistically significant at least at the 95% confidence level. Ensemble member 1 is shown for each.

Accepted for publication in *Journal of the Atmospheric Sciences.* DOI 10.1175/JAS-D-21-0227.1.

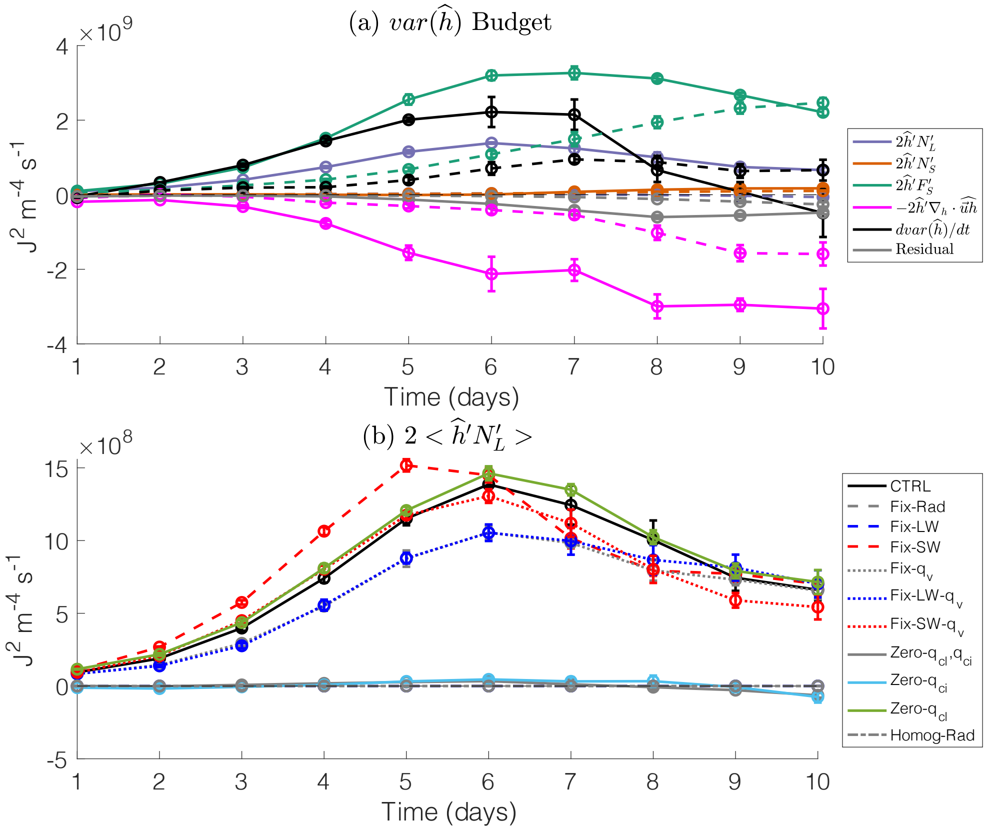

FIG. 11. (a) Daily mean, domain-mean var($\widehat{\mathrm{h}}$) budget for CTRL (solid lines) and Zero-q_{cl},q_{ci} (dashed lines), including contributions to the var($\widehat{\mathrm{h}}$) tendency from the longwave ($2\langle\widehat{h'N_L'}\rangle$; blue), shortwave ($2\langle\widehat{h'N_S'}\rangle$; red), surface flux ($2\langle\widehat{h'F_K'}\rangle$; green), and advective feedbacks ($-2\langle\widehat{h'}\nabla_h\cdot\widehat{\mathbf{u}h}\rangle$; pink). The variance tendency ($d\mathrm{var}(\widehat{h})/dt$; black) and the budget residual (gray) are also shown. (b) Daily mean longwave feedback, $2\langle\widehat{h'N_L'}\rangle$, in all simulations. Note that $2\langle\widehat{h'N_L'}\rangle$ is by definition zero in Fix-Rad, Fix-LW, and Homog-Rad. In both (a) and (b), the solid line shows the ensemble mean and the error bars show the ensemble range. Hourly means are noisier but have similar dependencies (not shown).

Accepted for publication in *Journal of the Atmospheric Sciences*. DOI 10.1175/JAS-D-21-0227.1.

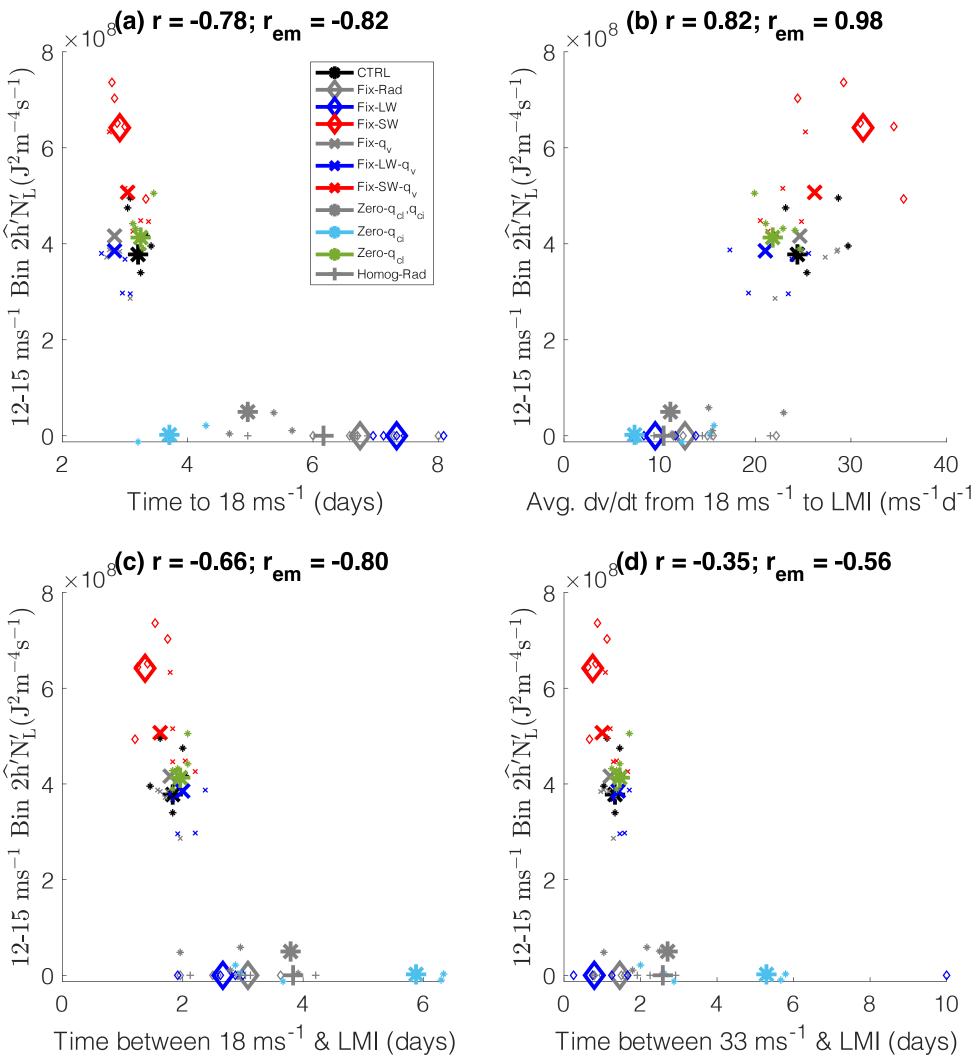

FIG. 12. Composite mean of the longwave feedback, $2\langle\widehat{h'N'_L}\rangle$, over times at which V_{max} is between 12-15 m s^{-1}, against (a) the time to reach tropical storm strength (18 m s^{-1}), (b) the average intensification rate (m s^{-1}d^{-1}) between the time of tropical storm strength and the lifetime maximum intensity (LMI), (c) the time to intensify from tropical storm strength to the LMI, and (c) the time to intensify from hurricane strength (33 m s^{-1}) to the LMI. A six-hour running mean is applied to V_{max} before computing the statistics. Note that $2\langle\widehat{h'N'_L}\rangle$ is by definition zero in `Fix-Rad`, `Fix-LW`, and `Homog-Rad`. The correlation coefficient is indicated across all simulations (r; small symbols) and across the ensemble means (r$_{em}$; large bold symbols); similar results are found when considering an individual ensemble member. All correlations are statistically significant at the 99% level except (d) for the ensemble mean, which is significant at the 90% level.

Accepted for publication in *Journal of the Atmospheric Sciences*. DOI 10.1175/JAS-D-21-0227.1.

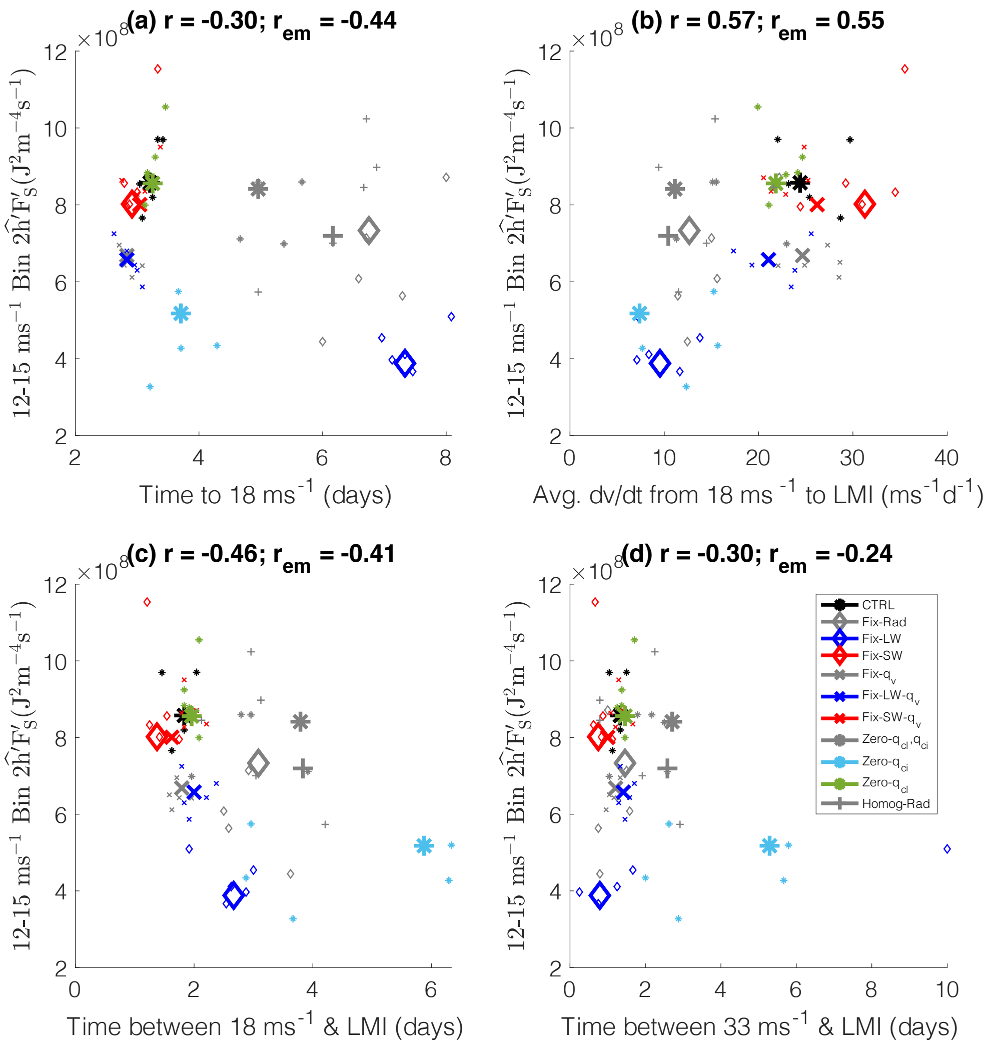

FIG. 13. Composite mean of the surface flux feedback, $2\langle\widehat{h'F'_K}\rangle$, over times at which V_{max} is between 12-12 m s^{-1}, against (a) the time to reach tropical storm strength (18 m s^{-1}), (b) the average intensification rate (m s^{-1}d^{-1}) b5tween the time of tropical storm strength and the lifetime maximum intensity (LMI), (c) the time to intensify from tropical storm strength to the LMI, and (c) the time to intensify from hurricane strength (33 m s^{-1}) to the LMI. A six-hour running mean is applied to V_{max} before computing the statistics. The correlation coefficient is indicated across all simulations (r; small symbols) and across the ensemble means (r$_{em}$; large bold symbols); similar results are found when considering an individual ensemble member. The correlations across all simulations are all statistically significant at the 95% level, while none of the correlations across the ensemble means are (except for (d), which is significant at the 90% level).

Accepted for publication in *Journal of the Atmospheric Sciences*. DOI 10.1175/JAS-D-21-0227.1.